Article

A Mathematical Spline-Based Model of Cardiac Left Ventricle Anatomy and Morphology §

Sergei Pravdin [1,2]

[1] Krasovskii Institute of Mathematics and Mechanics, Ural Branch of Russian Academy of Science, 620990 Ekaterinburg, Russia; sfpravdin@imm.uran.ru

[2] Ural Federal University, 19 Mira street, 620002 Ekaterinburg, Russia

§ This paper is an extended version of our paper published in S. Pravdin. A mathematical model of cardiac left ventricle anatomy and morphology. Abstracts of «Experimental and computational biomedicine»: Russian Conference with International Participation in memory of Professor Vladimir S. Markhasin. 2016. P. 25.

Abstract: Computer simulation of normal and diseased human heart activity requires a 3D anatomical model of the myocardium, including myofibres. For clinical applications, such a model has to be constructed based on routine methods of cardiac visualisation such as sonography. Symmetrical models are shown to be too rigid, so an analytical non-symmetrical model with enough flexibility is necessary. Based on previously made anatomical models of the left ventricle, we propose a new, much more flexible spline-based analytical model. The model is fully described and verified against DT-MRI data. We show a way to construct it on the basis of sonography data. To use this model in further physiological simulations, we propose a numerical method to utilise finite differences in solving the reaction-diffusion problem together with an example of scroll wave dynamics simulation.

Keywords: left ventricle; myofibre; myocardium structure; rule-based model; mathematical anatomy.

MSC: 92-08

1. Introduction

Integrative mathematical models of complicated hierarchic physiological systems, such as the heart, allow the use of a computational mathematical approach to describe these systems from the molecular level to the macrolevel, which characterizes the structure and functions of the whole heart and/or certain heart chambers, including the LV. In the framework of numerical experiments, a comprehensive analysis of such ventricular models provides a way to elucidate the mechanisms of normal and pathological heart performance; these models also provide a way to predict potential methods of effective therapy, such as correcting mechanical and electrical cardiac function disturbances.

Preferential paths for the propagation of an electrical excitation wave in the human ventricular myocardium are associated with muscle fibres in tissue. The speed of an excitation wave along a fibre is several times higher than that across the direction of a fibre. Thus, 3D simulation of electrophysiological and mechanical activity of the heart requires an anatomical model that includes a field of myofibre directions.

Recently, several models of the electrical and/or mechanical activity of the whole heart or its chambers have been proposed [1–12]. The most valuable of these are based on a detailed description of cardiac anatomy and the fibre orientation field, which is crucial for a correct representation of the physiological function of the heart.

In the existing literature, there are two approaches for modelling heart chamber architectonics, including the morphological pattern of myocardium fibre orientation. The approaches are more

complementary to each other than alternative ones. For convenience, we have roughly and non-rigorously assigned them as empiric and theoretical approaches.

In empiric approaches, fibre orientation is directly measured in the heart using various experimental techniques, and in theoretical approaches, fibre orientation is generated using algorithms.

Examination of individual hearts and empirical models

Important and useful empiric approaches are represented in several well-developed published models [13–15]. These models are based on the detailed experimental mapping of individual hearts. In current research, directions of fibres in the myocardium can be measured by different experimental methods. Particularly, the *Diffusion Tensor Imaging* (DTI) technique has been used to obtain images that show the fibre orientation and anisotropy of the heart [16–19]. Such measurements can be done with a spatial resolution of up to 0.3–0.5 mm and, in general, produce high-quality data, which can be used in computer-based models.

Another way of measuring anisotropy directly is the tedious histological study of fibre direction in 3D [20,21], where the researcher makes a series of parallel slices of the part of the heart under investigation. In every slice, angles of fibre slope are measured. When all the angular values are composed, the researcher obtains a full picture of the fibre directions in the organ.

The initial quantitative approache to describing animal and human heart anatomy was established by D. Streeter in 1960s [20]. It is worthy of note that all the approaches on fibre orientation in the human heart are either based on or use the results of Streeter's classical studies. Streeter not only measured fibre orientation in the heart, but also proposed several hypotheses on how this fibre orientation could be reproduced using geometrical transformations. However, for a long time Streeter's ideas were not implemented in a mathematical model.

The question of *laminar arrangement* in the muscular fibres and sheets is one of the basic matters in cardiac anatomy. Such an arrangement is hard to measure and is still under debate [21–23]. We have not attempted to include it in our present description.

Every directly measured dataset is connected to one concrete patient or laboratory animal and, thus, cannot be directly used for personalized heart models. Hence, there is a demand for algorithms which will allow existing data to be projected onto any geometry (see [18]) or which will allow researchers to generate such fibre orientation fields from any given geometric data.

At the same time, strictly speaking, any model built on the basis of a particular arrow map is a model of one particular heart as it is difficult to distinguish between the common properties of the heart of a given species and the individual specificity of the scanned heart sample. Of course, individual computational models of heart chamber architectonics built with the empirical approach may be developed further, up to the species model level. Correct averaging of data obtained via the mapping of individual heart samples will be necessary for this. Several promising works are focussing on this goal [24–27]. Models based on the empiric approach might, among other things, essentially contribute to the parameter verification of the models developed via the theoretical approach.

Each of the listed experimental methods allows researchers to obtain the fibre orientation field and use it to set up a model, and this approach is the best one to study a particular heart for which the measurements were performed. However, a researcher may not only need to study a given anisotropy but also to modify it, e.g. to study its effects on various electromechanical processes. In many cases, anatomy alone, not fibre orientation, is known, and some algorithms are needed to build up the anisotropy. Such algorithms are based on generic views of cardiac anatomy, which have been obtained through more than a century of cardiac research.

Peer-reviewed version available at Computation 2016, 4, 42; doi:10.3390/computation4040042

Theoretical models of cardiac anatomy

The theoretical approach to the modelling of heart chamber, e.g. the LV, architectonics arises from the attempt to clarify a general principle or governing rule that determines the orientation of the fibres in the ventricle wall. Such theoretical models may be especially useful when studying basic mechanisms of normal and pathologic heart performance.

The discovery of rotational anisotropy in the myocardium was one of the first fundamental findings in qualitative heart anatomy. The tangents to the myofibres turn, if we look at them transmurally, and the turning angle equals approximately 120°. Streeter compared this picture with a Japanese fan [20]. Torrent-Guasp suggested that we consider the myocardium of both ventricles as a 'flattened rope' or a band which has two endings and makes a few turns [28]. According to Streeter [20], myofibres are geodesic lines on a set of nested toroids, and outer toroids are more prolate while inner ones are more round. Besides this model, there are many models concerning a few myocardial layers (usually three, namely, superficial, middle and deep; see, for example, [29]). One can find a more detailed description of the history of cardiac qualitative anatomy in [30].

One group of models constructs the architectonics of myocardial fibres by using the analogy of muscular skeletal fibres. Different models include from one to four systems of myocardial bundles [31–35]. However, some researchers point to restrictions of the approach [36–38].

Another hypothesis to LV architectonics considers it as a kind of vascular musculature, where many junctions between the fibres exist [39–43].

One of the key questions concerning the LV myocardium is related to its layers – namely, their existence – and, if they exist, their number and positions. As a rule, models with sheets have a number of layers inserted one into another [29]. Nevertheless, a layers-based model exists in which the number of sheets is indefinite and the LV is not divided to internal and external parts. The model in question is from an early work [28], published in 1973, in which Torrent-Guasp proposed a hypothesis on how cardiac fibre orientation could be reproduced using geometrical transformations. However, this idea has never been formulated in mathematical terms.

Let us now discuss mathematical models of the heart. Theoretical approaches to cardiac architectonics include rule-based methods [44–46] and the mapping of fibres from animal hearts to human heart geometry [47]. One of the most recent rule-based methods is a Laplace–Dirichlet algorithm [46], which takes a noisy DTI-derived fibre orientation field as input data and yields, firstly, the transmural and apicobasal directions for the entire myocardium and, secondly, a smooth and continuous fibre orientation field. Another approach was used by Peskin, who derived the fibre orientation field from the principles of mechanical equilibrium [48].

Chadwick considered a cylindrical LV model and specified the helix angle linearly depending on the position of the point in the LV wall [49]. A spheroidal LV model, which involved the linear dependence of the helix angle on the distance between the point and the endocardium, was proposed by Beyar et al. in [2].

Another theoretical approach was created by Arts et al. in 1992 [50]. Their model was an ellipsoidal LV with a piecewise quadratic law for helix angle change. The mechanical adaptational principle suggested by Arts et al. in 1982 [51] was used to quantify the orientation of muscle fibres via the helix fibre angle distribution.

Relation to other anatomical ventricular models

Torrent-Guasp in [28] suggested that the LV can be represented as a set of embedded surfaces, i.e. muscular layers, covered by curves representing the myofibres. This idea was illustrated using Pettigrew's proposal [52] of these surfaces having the form of a planar semicircle with a number of curves drawn on the semicircle. The sheets thereafter were transformed into conical surfaces. Finally, the heart was considered as a family of such conical surfaces inserted into each other. It may be noted that Streeter mentioned the importance of these ideas but did not formalize them.

The present work develops two analytical LV models based on Pettigrew's anatomical concept. One of the models is axisymmetric [53]. The other model is built on power functions and is not symmetric [54]. Heart anatomy was described in these works using a family of inserted non-conical surfaces, which allowed us to represent the smooth geometry of the LV properly. A family of lines on these surfaces was used to represent cardiac fibres. The entire model was expressed in terms of analytical functions.

Our experience shows that in many situations, a well-fitting non-symmetric LV model cannot be made using the approach from [54]. We faced this when we tried to make «power-function» models using sonography and tomography data of human hearts. The limitation of the approach is that the LV model cannot fit shapes of some real hearts accurately enough.

The new model uses splines instead of power functions and, as we will show in this paper, is flexible enough to fit real medical visualisation data. At the same time, the new model uses analytical calculations, so some of the derivatives necessary for solving reaction-diffusion systems can be found exactly. In the proposed model, both anatomy and fibre direction field are defined analytically. We calculate fibre slope angles in a local coordinate system and compare them with *in vitro* experimental data on human hearts.

In the next Section, we describe the details of our model construction. In Sections 3 and 4, we compare its output with experimental measurements of anisotropy in the human and canine LV. In Section 5, we propose a technique for constructing a model based on sonography data, which is especially important for clinical applications. Sections 6 and 7 provide a numerical method for simulating the electrophysiological activity of the LV and an example of the usage of the numerical method. Finally, Section 8 is discussion on the results obtained.

2. Construction of the LV model

In order to define the LV form, we use a special coordinate system (γ, ψ, ϕ), where the variable $\gamma \in [0,1]$ corresponds with position of a point in the LV wall layer: $\gamma = 0$ is the endocardium, $\gamma = 1$ is the epicardium, $\psi \in [0, \pi/2]$ is an analogue of latitude, $\psi = 0$ is the upper plane part of the LV model (fibrous ring and valve zone), $\psi = \pi/2$ is the LV apex, and $\phi \in [0, 2\pi)$ is an analogue of longitude.

Initial data for the model construction are

1. meridians ϕ_i, $i = 0, 1, \ldots n-1$, where measurements are taken;
2. coordinates $\rho^{epi}_{i,j}$, $z^{epi}_{i,j}$, $i = 0, 1, \ldots n-1$, $j = 0, 1, \ldots n^{epi}_i - 1$, of *marked* points on the epicardium;
3. coordinates $\rho^{endo}_{i,j}$, $z^{endo}_{i,j}$, $i = 0, 1, \ldots n-1$, $j = 0, 1, \ldots n^{endo}_i - 1$, of *marked* points on the endocardium.

Now we describe our algorithm to construct the LV model. First, for each meridian of the epicardium, we connect the marked points by an interpolation curve (Fig. 1). We obtain a set of n curves in this step. Second, for each latitude ψ, we connect the n points on the curves by a closed interpolation curve. Algebraically, this means that we use a periodic spline. We obtain an epicardial surface in this step. Next, we do the same for the endocardium and, finally, we fill the space between the epi- and endocardium by a linear function of γ.

This schema can be formalised using the following equations. To transform the special coordinates into cylindrical ones (ρ, ϕ, z), we use a simple formula for z-coordinate transformation:

$$z(\gamma, \psi) = Z - (Z - h\gamma) \sin \psi, \tag{1}$$

where Z is the LV height, and h is the LV wall thickness at the apex. Using this formula, we calculate ψ-coordinates of the marked points:

$$\psi(\gamma, z) = \arcsin\left(\frac{Z - z}{Z - h\gamma}\right). \tag{2}$$

Preprints (www.preprints.org) | NOT PEER-REVIEWED | Posted: 20 October 2016 doi:10.20944/preprints201608.0080.v2

Peer-reviewed version available at Computation 2016, 4, 42; doi:10.3390/computation4040042

As mentioned above, $\gamma = 0$ on the epicardium, and $\gamma = 1$ on the endocardium.

In each section ϕ_i on the epicardium (endocardium), we make an epicardial (endocardial) curve

$$\rho^{epi}(\psi, \phi_i) = \text{spline}(\psi; \psi^{epi}_{i,j} \mapsto \rho^{epi}_{i,j}), \qquad \rho^{endo}(\psi, \phi_i) = \text{spline}(\psi; \psi^{endo}_{i,j} \mapsto \rho^{endo}_{i,j}). \tag{3}$$

Here, spline is a cubic spline with zero second derivative at the endpoints. The notation $\text{spline}(x; x_i \mapsto y_i)$ means a spline constructed by two given arrays of data, x_i as an argument and y_i as a response variable. Then, we interpolate to obtain a surface between the curves:

$$\rho^{epi}(\psi, \phi) = \text{spline}(\phi; \phi_i \mapsto \rho^{epi}(\psi, \phi_i)), \qquad \rho^{endo}(\psi, \phi) = \text{spline}(\phi; \phi_i \mapsto \rho^{endo}(\psi, \phi_i)). \tag{4}$$

Here, we use a periodic cubic spline. And finally, we fill the entire LV wall:

$$\rho(\gamma, \psi, \phi) = \rho^{epi}(\psi, \phi)(1 - \gamma) + \rho^{endo}(\psi, \phi)\gamma. \tag{5}$$

Usually, if n meridional sections are considered, the angles between them are uniform, so $\phi_i = i\pi/n$, $i = 0, 1, \ldots n - 1$.

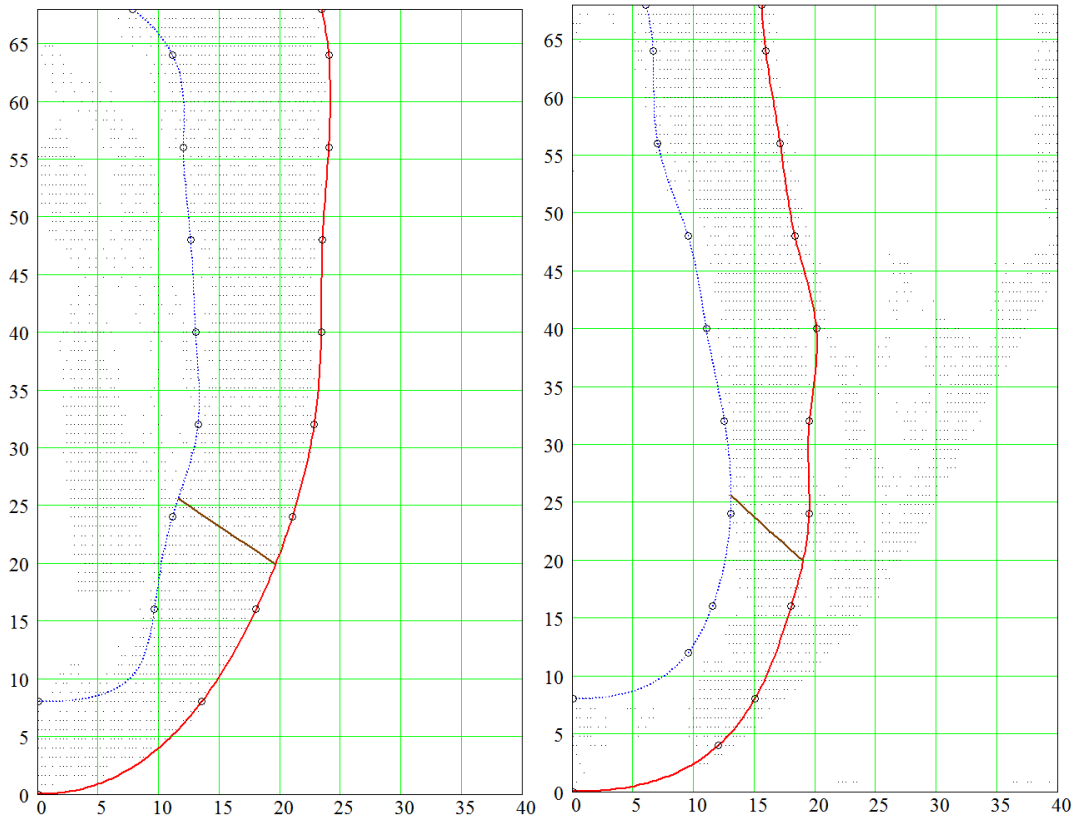

Figure 1. Vertical (meridional) sections of the LV free wall (on the left) and the IVS (on the right) of a human heart. The points represent DT-MRI data; the solid red line represents the model epicardium; the dashed blue line represents the model endocardium. The circles show the interpolation (marked) points given by a user. The horizontal axis is ρ; the vertical axis is z. On the right panel, we see a papillar muscle in the RV cavity (vertical one, $\rho = 25 \ldots 45$ mm) and an RV free wall (inclined).

Preprints (www.preprints.org) | NOT PEER-REVIEWED | Posted: 20 October 2016 doi:10.20944/preprints201608.0080.v2

Peer-reviewed version available at Computation 2016, 4, 42; doi:10.3390/computation4040042

2.1. Spiral surfaces

Hierarchically, the LV model is subdivided into muscle layers. In its turn, each layer is filled by myofibres. All the layers have a spiral-like shape so we call them «spiral surfaces» (SS). These surfaces have the same equation in special coordinates:

$$\phi(\gamma, \phi_{\min}, \phi_{\max}) = \phi_{\min} + \gamma\phi_{\max}, \tag{6}$$

where $\phi_{\max}$ is the SS twist angle (which is the same for all SS), and different values of $\phi_{\min} \in [0, 2\pi)$ determine different surfaces. The equation of the SS in the cylindrical coordinates is shown below (see (5), (1)).

$$\rho_{sp}(\psi, \phi, \phi_{\min}) = \rho\left(\frac{\phi - \phi_{\min}}{\phi_{\max}}, \psi, \phi\right); \tag{7}$$

$$z_{sp}(\psi, \phi, \phi_{\min}) = z\left(\frac{\phi - \phi_{\min}}{\phi_{\max}}, \psi\right). \tag{8}$$

2.2. Filling a spiral surface with fibres

We have utilised J. Pettigrew's proposal [52] as we did in our previous models [53,54]. This proposal has been chosen because it can be formalised easily, and it describes both myofibres and sheets. Myocardial fibres are obtained as images of chords $Y = \text{const}$, $Y \in [0, 1)$ of sector $\mathrm{P} \le 1$, $\Phi \in [\pi\gamma_0, \pi\gamma_1]$ (the chords are parallel to the diameter $Y = 0$) on the SS (Fig. 2). Here, γ_0 and γ_1 $(0 \le \gamma_0 < \gamma_1 \le 1)$ are parameters necessary to fit the sub-epicardial and sub-endocardial fibre angles. The parameter of any chord is the polar angle $\Phi \in [\Phi_0, \Phi_1]$, where $\Phi_0 = \max(\arcsin Y, \pi\gamma_0)$ and $\Phi_1 = \min(\pi - \arcsin Y, \pi\gamma_1)$. The mapping of a chord point (P, Φ) to an SS point is defined by the formulae below (Fig. 3):

$$\gamma(\Phi) = \frac{\Phi - \pi\gamma_0}{\pi(\gamma_1 - \gamma_0)},$$
$$\psi(\mathrm{P}) = (1 - \mathrm{P}) \cdot \frac{\pi}{2}.$$

For instance, if $\gamma_0 = 0$ and $\gamma_1 = 1$, the semicircle diameter is transformed into a fibre that begins on the basal epicardium, descends to the apex $(\Phi = \pi/2)$, then ascends and ends on the basal endocardium. Images of shorter chords are located closer to the LV base and have shorter lengths.

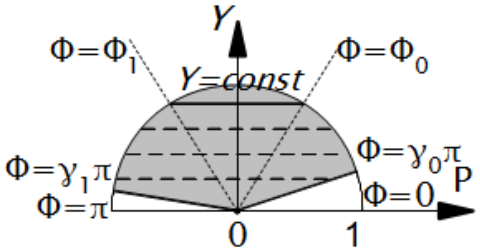

Figure 2. Horizontal chords on the sector $\mathrm{P} \le 1$, $\Phi \in [\pi\gamma_0, \pi\gamma_1]$. Here, Φ_0 and Φ_1 are polar angles of the right and left chord ends, respectively. Parameter $\gamma_0 = 0.1$ and $\gamma_1 = 0.95$.

2.3. Fitting the LV form

In the paper [54], a fitting of the more rigid model to a real canine heart dataset was done with satisfactory results. Yet, fitting the dataset of a human heart into that model was less successful, partially due to the limitations of the model's parameters. In this study, the same dataset of the human heart was used for the flexible model. The dataset is accessible online at

Preprints (www.preprints.org) | NOT PEER-REVIEWED | Posted: 20 October 2016 doi:10.20944/preprints201608.0080.v2

Peer-reviewed version available at Computation 2016, 4, 42; doi:10.3390/computation4040042

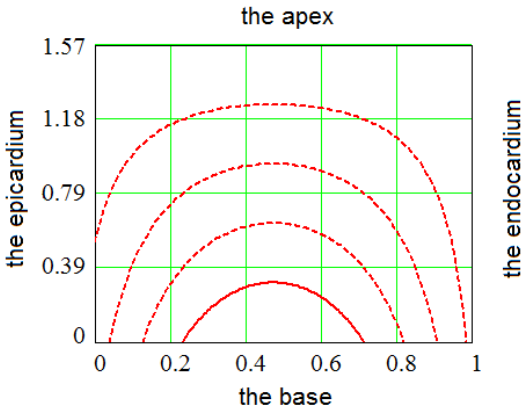

Figure 3. Images of the sector chords in (γ, ψ) coordinates. The horizontal axis is γ, and the vertical axis is ψ. Parameter $\gamma_0 = 0.1$ and $\gamma_1 = 0.95$.

`http://gforge.icm.jhu.edu/gf/project/dtmri_data_sets/docman/`

The fitting procedure began with finding the LV axis Oz. Then, we sectioned the LV by $N = 12$ meridional half-planes $\phi_i = 2\pi i/N$, $i = 0, 1 \ldots N-1$, passing this axis, and we manually marked points on the epi- and endocardium in each section. The mean numbers of points were 10 for the sub-endocardium and 11 for the sub-epicardium. In total, taking into account the coincidence of two apical points in all the sections, there were 227 points. After setting the points, we used periodic cubic ϕ-splines and cubic ψ-splines.

3. Methods for model and experimental data comparison

In the work [54], the theoretical model and experimental data were compared along normals to epicardial meridional sections as described in [20]. However, this method is not useful: normals do not have to intersect the endocardium, and they may intersect each other, so the task of finding a normal passing through a point may result in multiple solutions. In the present article, we use the special coordinates to construct straight *pinning* lines that do not intersect each other and always intersect the endocardium. These lines have a simple equation: $\psi = \text{const}$, $\phi = \text{const}$.

We will now describe the comparison procedure. To compare angles along such a pinning line, one needs to specify a point A on the epicardium. Let its special coordinates be $\gamma = 0$, $\psi = \psi^*$ and $\phi = \phi^*$. Let us consider a corresponding meridional section $\phi = \phi^*$ of the model, semiplane Π. The line lies in Π and intersects the endocardium at a point B, having coordinates $\gamma = 1$, $\psi = \psi^*$ and $\phi = \phi^*$. On the segment AB, we set k unidistant points, including its ends, so that $A = A_1, A_2, \ldots, A_k = B$. The position of a point A_i on the segment AB is defined by the variable

$$\mathrm{x}_i = \frac{A_i B}{AB}$$

(for the endocardium $\mathrm{x} = 0$, for the epicardium $\mathrm{x} = 1$). We have to draw an SS through every point $A_i(\gamma_i = (i-1)/(k-1), \psi^*, \phi^*)$. The problem of finding such an SS is reduced to solving the SS equation (6) with respect to $\phi_{\min}$:

$$\phi_{\min} = \phi^* - \gamma_i \phi_{\max}.$$

Strictly speaking, there can be no points from the tomogram exactly on semiplane Π; therefore, we selected points lying no further than $\Delta = 1$ mm from the straight line AB and inside the dihedral angle $|\phi - \phi^*| \le \Delta_\phi = 0.1$ rad$= 5.7^\circ$.

Streeter proposed specifying fibre direction using a local coordinate system (u, v, w) and two angles, 'true fibre angle' α and 'helix angle' α_1 [20, p. 78] (see Fig. 6); these angles are sufficient for specifying the direction of a fibre at a particular point. The true fibre angle reflects fibre direction

Peer-reviewed version available at Computation 2016, 4, 42; doi:10.3390/computation4040042

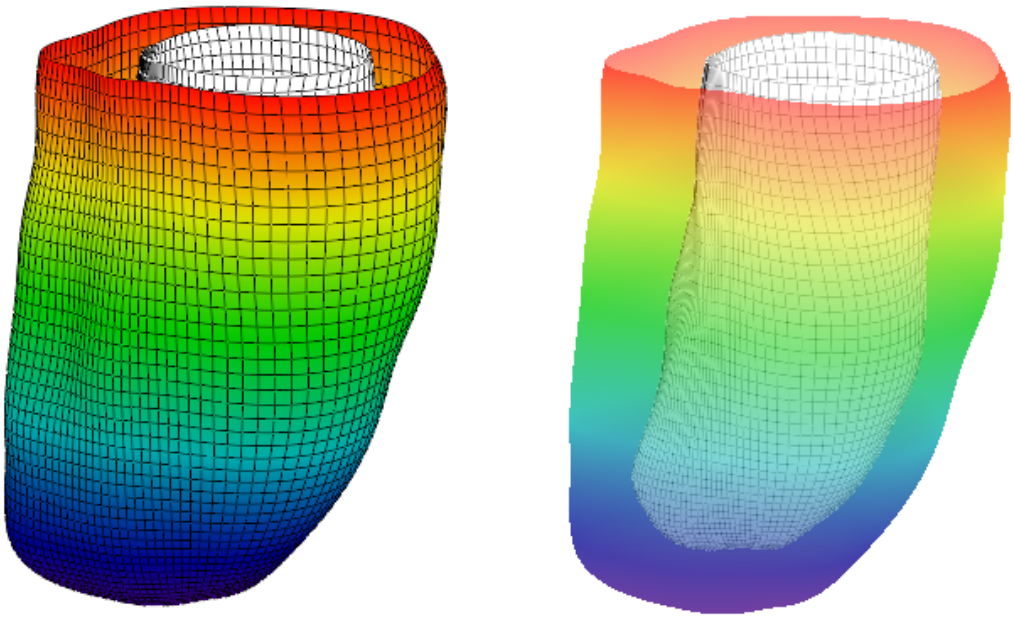

Figure 4. Epicardial and endocardial surfaces of the model that was constructed based on DT-MRI data. On the left, the epicardium is opaque. On the right, the epicardium is semi-transparent. Colour shows z-coordinates.

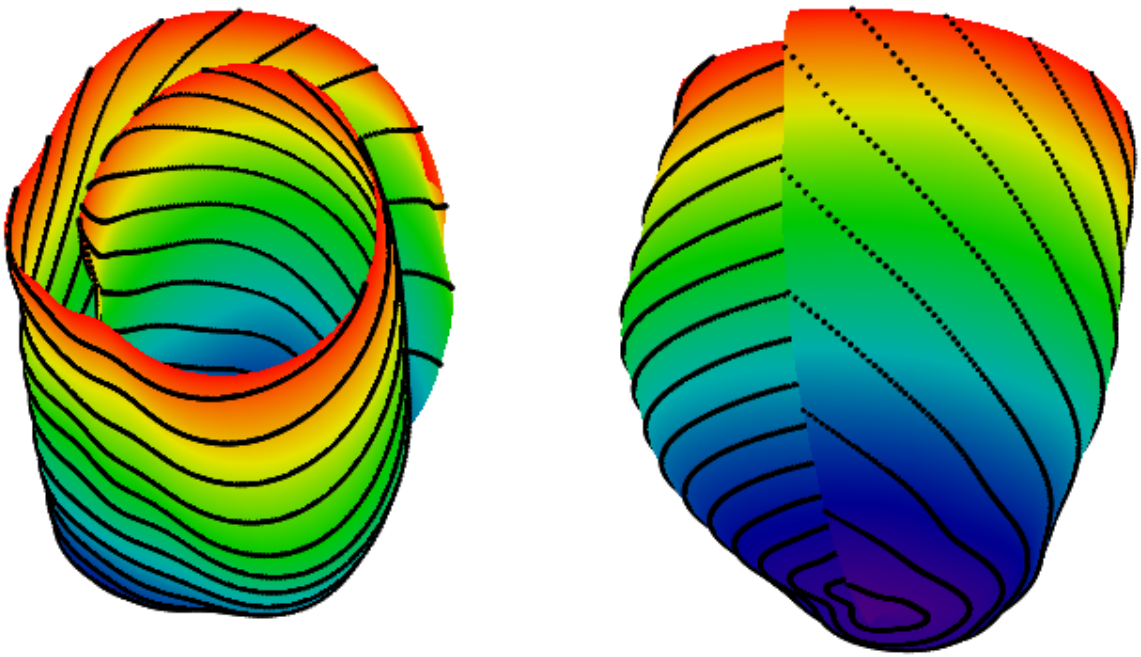

Figure 5. A spiral surface (SS) with fibres on it. Two views are shown. The left of the figure depicts a view from the top and side of the SS, while the right of the image provides a side view with the mid-myocardial part on the left and the epicardial layer on the right. Colour shows z-coordinates.

Preprints (www.preprints.org) | NOT PEER-REVIEWED | Posted: 20 October 2016 doi:10.20944/preprints201608.0080.v2

Peer-reviewed version available at Computation 2016, 4, 42; doi:10.3390/computation4040042

totally, with both helix and transverse components, while the helix angle neglects the transverse part. The axis u is a normal to the epicardium pointed away from the LV; w is a meridian, i.e. an epicardial tangent lying in a meridional semiplane and pointed upwards, and v is a parallel, i.e. vector $w \times u$. Angle $\alpha \in [0, \pi/2]$ is between a fibre and the parallel, and angle $\alpha_1 \in [-\pi/2, \pi/2]$ is between the fibre projection on the plane uv and the parallel.

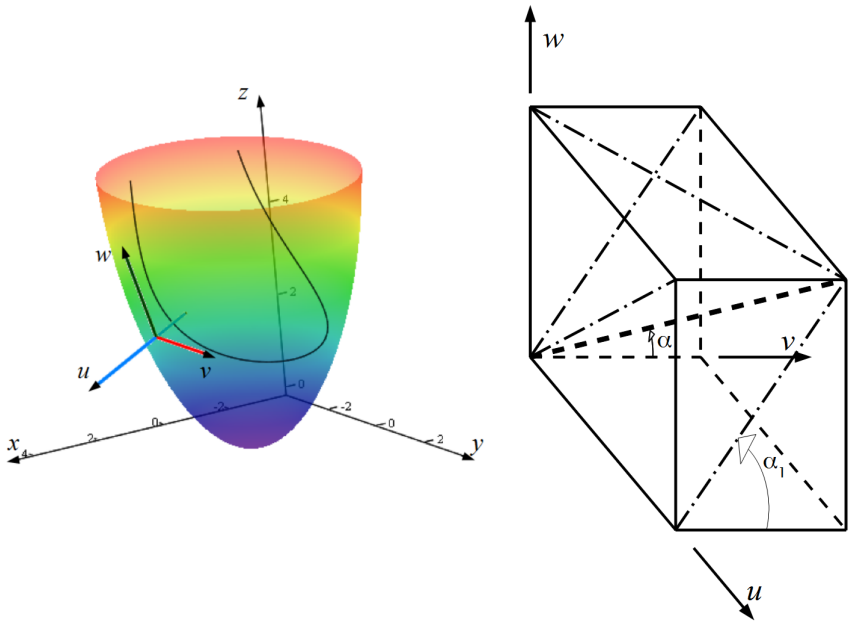

Figure 6. The definition of the local coordinate system is shown on the left of the image. $Oxyz$ is the global Cartesian coordinate system. The blue axis is normal, u, to the epicardium. The red axis is parallel tangent, v. The dark green axis is meridian tangent, w. The colourful surface is the epicardium; the colour depends on altitude z. The curve inside is a model fibre and it does not lie on the epicardium. The normal axis intersects the curve at a point. On the right, the definitions of the true fibre angle α and the helix angle α_1 are shown. The thick, dashed line is a tangent to a myofibre segment constructed at the origin of the coordinates. The dashed-and-dotted lines are projections of the myofibre tangent.

We compared the two angular characteristics of fibre directions with the experimental data for a human heart in two meridians (one meridian lies in the LV free wall, another lies in the IVS) in upper, middle and lower parts of the LV wall.

4. Results of comparing the model with DT-MRI data

In this Section, we compare the directions and angles of myocardial fibres in the model and DT-MRI data of one human and one canine hearts.

4.1. Comparison of the model with human heart data along straight pinning lines

The following parameter values, which are common for all meridians, were used: LV height $Z = 68$ mm, LV wall thickness at the apex $h = 8$ mm, SS twisting angle $\phi_{\max} = 3\pi$, endocardial fibre parameter $\gamma_0 = 0.13$ and epicardial fibre parameter $\gamma_1 = 0.9$.

Graphs of the dependency of angles α, α_1 on a point position on pinning lines are shown in Figs. 7–12. We will now analyse the results obtained.

At the upper and middle LV areas (e.g., Figs. 7 and 8, A), one can see that the vertical axis does not go through the centre of the horizontal LV sections, but it is situated closer to the IVS. The axis is

positioned there because it must go through the apical LV area, and the LV apex projection to its basal plane is not situated at the centre of the base. If one moves the axis to the base centre, then the apex is far from the axis in one of the meridional sections; therefore, we cannot fit the LV wall shape using the central position of the axis.

Let us consider the fibre slope angles in one of the LV free-wall meridians. In the upper LV part (see Fig. 7), the true fibre angle α (panel *C*) in the model accurately reproduces the DT-MRI data. Angle α descends from 75° on the endocardium to approximately 15° at the middle of the wall, then it reaches 65° on the epicardium. The helix angle (panel *D*) in the model is also quite close to the experimental data. The middle part of the free wall, which is determined by height (see Fig. 8), shows an essentially large dispersion of the both angles' values in the subendocardial zone $(x < 0.2)$. These angles' values are similar to those in the basal zone, so the model can reproduce them well. The angles at the lower part of the LV free wall (see Fig. 9) are predicted by the model with slightly lesser accuracy.

In the upper part of the IVS (see Fig. 10), the model behaves in a different way than the experimental data. In the middle part of the IVS (see Fig. 11), the model reproduces the angles reasonably accurately. Fig. 12 shows that the model simulates the angles in the interior part of the myocardium better than in the exterior part.

The transmural variation of angle α is parabolic both in the DT-MRI data and in the model. This angle is locally maximal at the subendo- and subepicardium, and it is minimal but not 0 at the middle of the wall, where the helix angle is 0. Angle α is not 0 there due to the traverse fibre angle.

The dashed black lines in Figs. 7–12 demonstrate the results of another modelling approach described in [46]. We see that the functions are linear with respect to x, and the angles do not depend on the region. Bayer et al.'s model has 0 transmural angle (traverse angle α_3 in Streeter's notation), so its angle $\alpha = |\alpha_1|$.

If one considers the fibres in the radial direction, our model (like the model from [53]) imitates the distinctive arrangement of fibres in the ventricular wall (see [53], Fig. 14). As we mentioned above, this arrangement was called the "Japanese fan" by Streeter (see [20], Fig. 42, *C*).

Preprints (www.preprints.org) | NOT PEER-REVIEWED | Posted: 20 October 2016 doi:10.20944/preprints201608.0080.v2

Peer-reviewed version available at Computation 2016, 4, 42; doi:10.3390/computation4040042

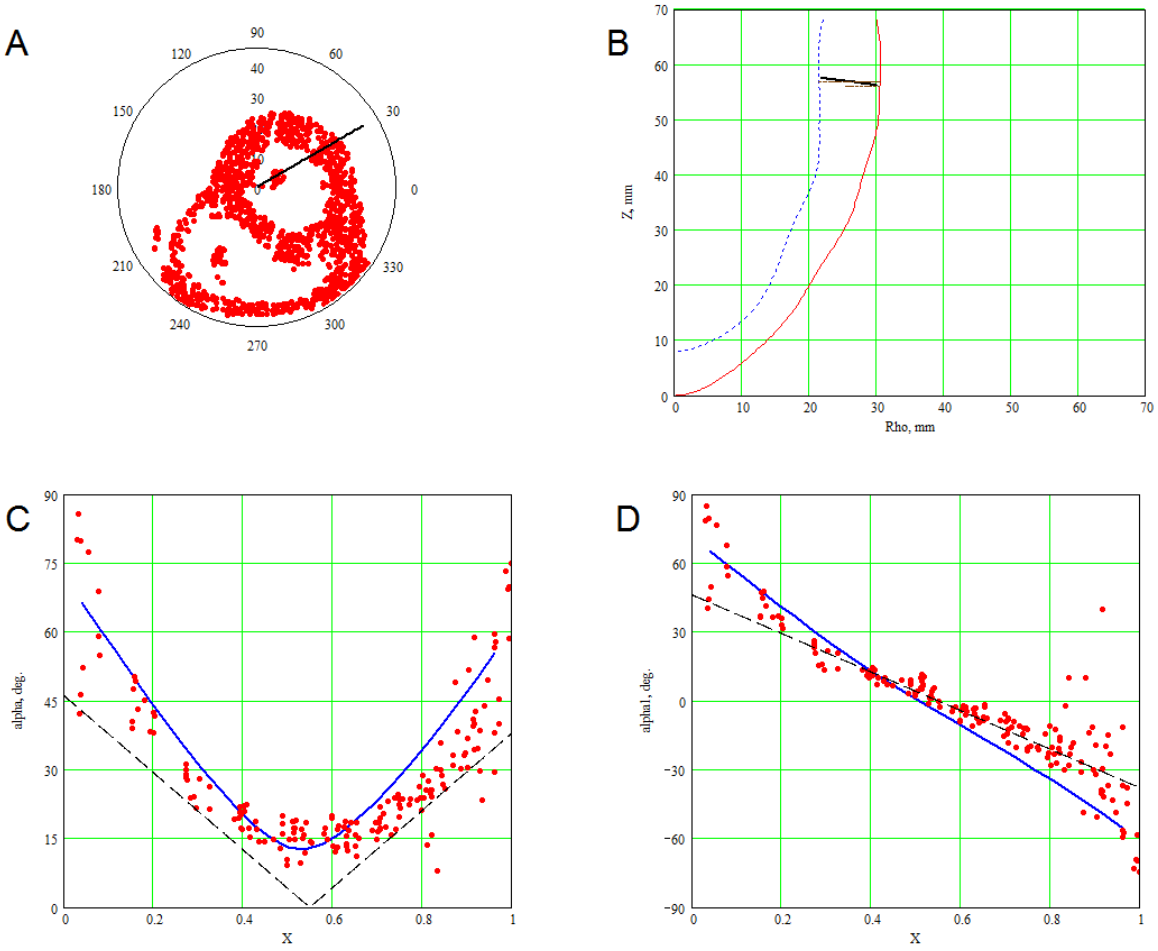

Figure 7. Fibre angles in the model and in the experimental data. The basal area ($\psi = 10^{\circ}$) of the LV free wall is shown. *A* is a horizontal LV section. The points are myocardial points from a human heart DT-MRI scan. *B* is a meridional LV section. The solid (dashed) curve is the model epicardium (endocardium), and the points are myocardial points from the DT-MRI scan. *C* and *D* show the angles α and α_1, respectively. The *X*-axis displays the position of points in the wall depth; 0 corresponds to the endocardium, and 1 corresponds to the epicardium. The points show the experimental data, while the solid curves show our model data, and the dashed curves display results yielded by the model from [46].

Preprints (www.preprints.org) | NOT PEER-REVIEWED | Posted: 20 October 2016 doi:10.20944/preprints201608.0080.v2

Peer-reviewed version available at Computation 2016, 4, 42; doi:10.3390/computation4040042

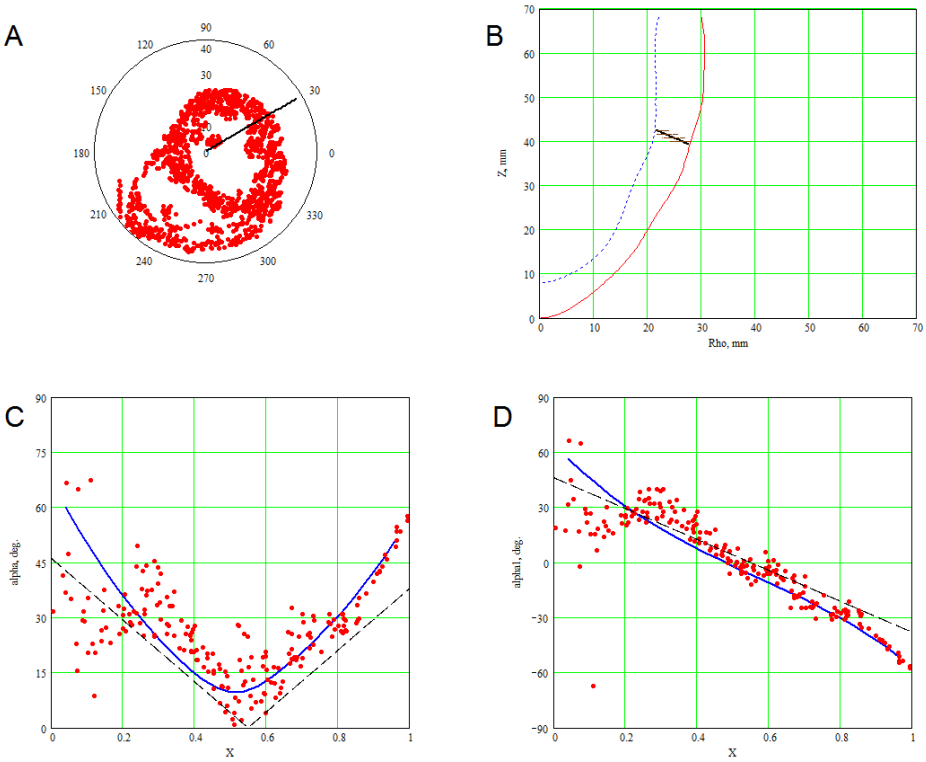

Figure 8. Fibre angles in the model and experimental data. The LV free wall in the middle area ($\psi = 25°$) is shown. The conventional signs are the same as in Fig. 7.

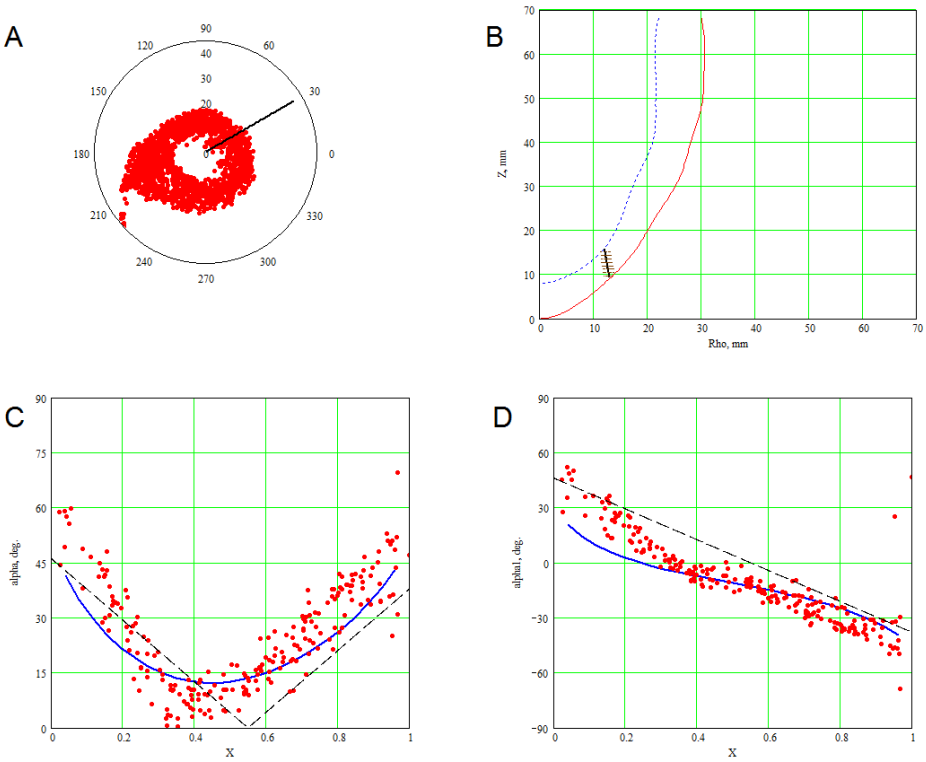

Figure 9. Fibre angles in the model and experimental data. The LV free wall in the apical area ($\psi = 60°$) is shown. The conventional signs are the same as in Fig. 7.

Preprints (www.preprints.org) | NOT PEER-REVIEWED | Posted: 20 October 2016 doi:10.20944/preprints201608.0080.v2

Peer-reviewed version available at Computation 2016, 4, 42; doi:10.3390/computation4040042

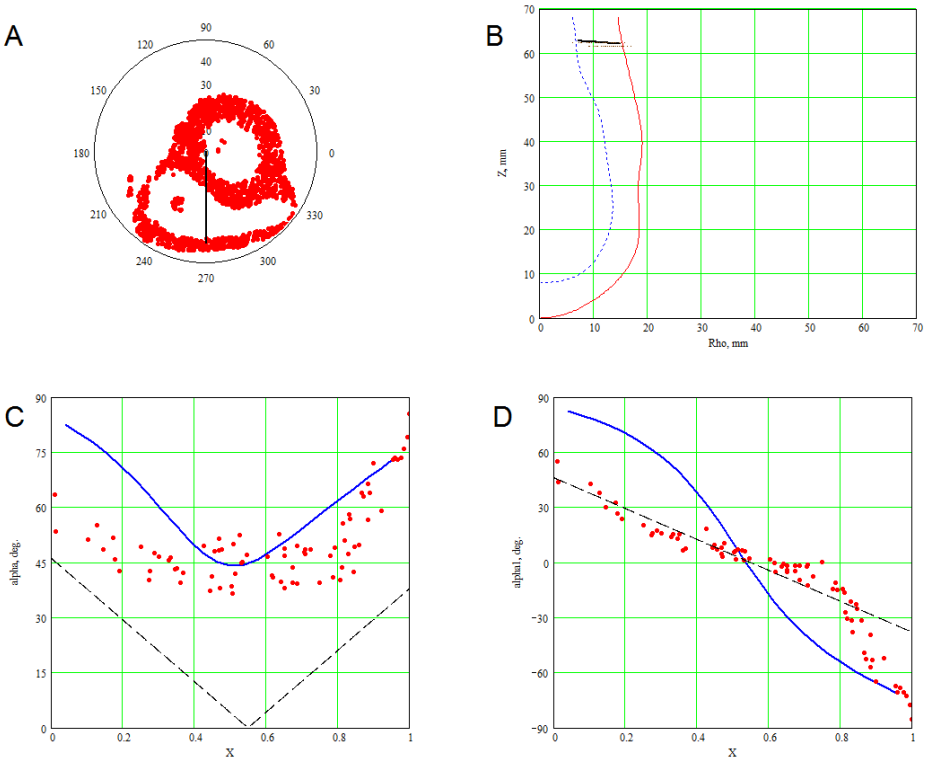

Figure 10. Fibre angles in the model and experimental data. The IVS in the basal area ($\psi = 5°$) is shown. The conventional signs are the same as in Fig. 7.

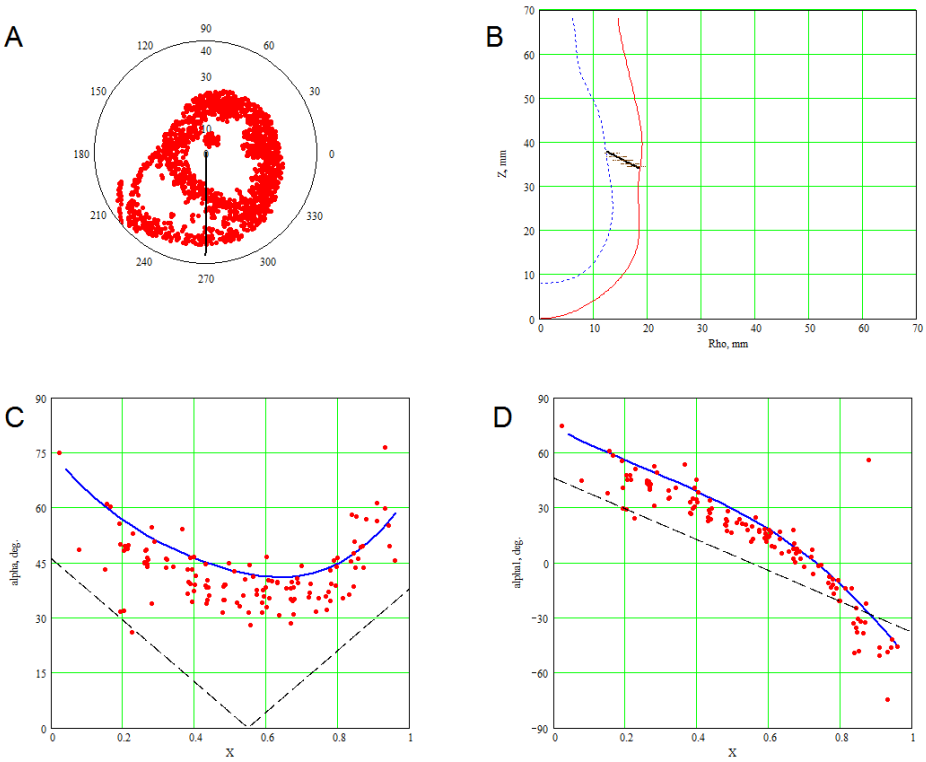

Figure 11. Fibre angles in the model and experimental data. The IVS in the middle area ($\psi = 30°$) is shown. The conventional signs are the same as in Fig. 7.

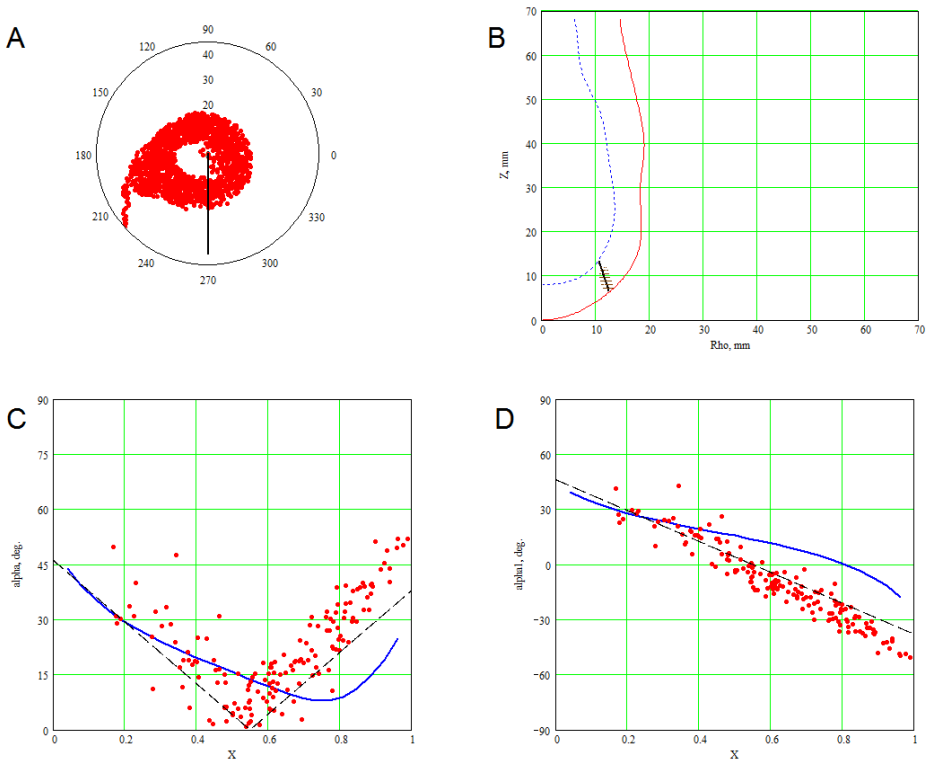

Figure 12. Fibre angles in the model and experimental data. The IVS in the apical area ($\psi = 65°$) is shown. The conventional signs are the same as in Fig. 7.

Preprints (www.preprints.org) | NOT PEER-REVIEWED | Posted: 20 October 2016 doi:10.20944/preprints201608.0080.v2

Peer-reviewed version available at Computation 2016, 4, 42; doi:10.3390/computation4040042

4.2. 3D verification

We compared the fibre directions of the human tomography dataset and the model in all DT-MRI points located inside the model LV wall, and we made a histogram of the results (Fig. 13). The mean angle between the two directions is 21.1° and the median is 15.2°. The standard deviation is 18°.

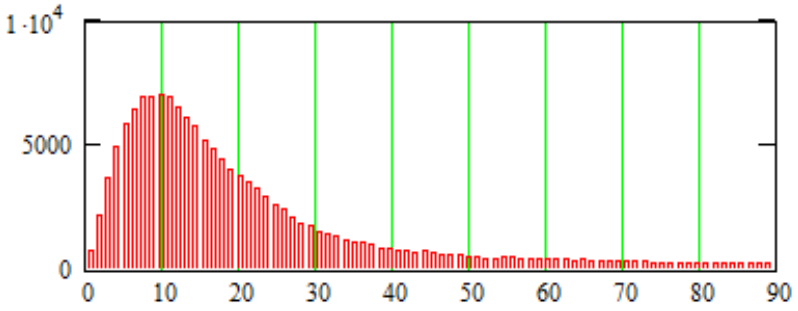

Figure 13. Histogram of angles between fibres in experiment and model data. The human heart dataset is used. X-axis is the angle; Y-axis is the number of points in the segments; the segment $[0, 90°]$ was divided into 100 segments of equal length.

Also, we used our model to fit a canine DT-MRI dataset, which is accessible through the link given in Section 2.3. The following parameter values, which are common for all meridians, were used: LV height $Z = 90$ mm, LV wall thickness at the apex $h = 12$ mm, SS twisting angle $\phi_{\max} = 3\pi$, endocardial fibre parameter $\gamma_0 = 0.18$ and epicardial fibre parameter $\gamma_1 = 0.9$. A 3D comparison of the dataset and the model was performed. This comparison showed the following results: mean 19.5°, median 16.1°, standard deviation 14.1°, which is very close to the human heart comparison.

The degree of error in the angles consists of two parts. One of them is the modelling error caused by inaccuracies in the model. This error can be seen in Figs. 7–12, where the blue curves are out of the red point clouds. The second part is caused by errors of measurement and by the dispersion of data. Even if a blue curve is in the middle of a point cloud, such errors accrue. To identify these parts of errors, we partly averaged the true fibre angle (α) and helix angle (α_1) data using the Smoothn function in Matlab [55], so we obtained data without outliers. The averaging is controlled by the smoothing parameter $s \geq 0$. If $s = 0$, the algorithm makes no changes in the input data. The noise in the data diminishes with the growth of s. Full averaging was impossible because an increase in the smoothing parameter above $s \approx 5$ led to an oversmoothing without an essential noise reduction. We used $s = 5$, and the results of the 3D comparison are shown in Tables 1 and 2.

Table 1. Statistics of the error in the true fibre angle.

True fibre angle	**Canine**		**Human**	
	raw data	averaged	raw data	averaged
mean	12.3°	10.9°	12.5°	10.1°
median	9.2°	8.7°	8.8°	7.8°
st. dev.	10.8°	9.1°	12.2°	9.2°

Table 2. Statistics of the error in the helix angle.

Helix angle	Canine		Human	
	raw data	averaged	raw data	averaged
mean	15.2°	12.3°	18.9°	13.3°
median	11.0°	9.8°	12.1°	10.2°
st. dev.	16.5°	9.8°	22.6°	11.5°

We can conclude that the partial averaging of the input data decreases the error sufficiently. The mean error in the fibre angles is about 10–15° for the data without outliers.

5. Constructing a model based on sonography data

The proposed model of the LV form can be constructed based on sonography data. We made one such measurement using data from two- and four-chamber views of one patient's heart. In Fig. 14, we show a comparison of two models: the old model based on power functions and the present spline-based one. The model was made using 44 marked points, from which 22 were endocardial and 22 were epicardial. Since the posterior (right on the image) part of the LV wall has a complex curved shape, it cannot be approximated accurately by the first model, but it can be well approximated by the second one. The anterior (left on the image) part of the LV wall has a simpler shape, so both models can be fitted into it well.

6. Numerical method for solving reaction-diffusion systems on the model

Electrophysiological processes in the myocardium are usually simulated using reaction-diffusion systems of partial differential equations. In the monodomain case, they are

$$\dot{u} = \operatorname{div}(D \operatorname{grad} u) + f(u, \vec{v}), \tag{9}$$

$$\dot{\vec{v}} = \vec{g}(u, \vec{v}). \tag{10}$$

Here, u is the transmembrane potential, $\vec{v}$ is the vector of other phase variables (its components differ in different models), the diffusion matrix D has elements $D_{ij} = D_2\delta^{ij} + (D_1 - D_2)w_i(\vec{r})w_j(\vec{r})$, $i, j = 1, 2, 3$, and $\vec{w}$ is the unit vector of fibre direction.

The boundary condition of zero flux of the potential through the myocardial boundary looks like

$$\vec{n} D \operatorname{grad} u = 0, \tag{11}$$

where $\vec{n}$ is a normal vector to the boundary. In the case of complex cardial shape, implementation of the boundary condition is difficult, and it requires either a special method of Laplacian computation near the boundary in Cartesian coordinates or a special coordinate system where the boundaries are coordinate surfaces.

The LV base, epicardium and endocardium are just coordinate surfaces in the special coordinates linked with this model. Indeed, the base has the equation $\psi = 0$, while the equation $\gamma = \text{const}$ describes the epicardium and endocardium. For the symmetrical LV model, we proposed an algorithm [57] which has been used in a study of scroll wave dynamics [58]. For the previous (power-functions based) non-symmetrical model [54], a modified algorithm has been described elsewhere [59]. That algorithm can be used in the present case as well without any changes. However, since it was not published in English, we depict its dissimilarity with the symmetrical-case method briefly here.

Preprints (www.preprints.org) | NOT PEER-REVIEWED | Posted: 20 October 2016 doi:10.20944/preprints201608.0080.v2

Peer-reviewed version available at Computation 2016, 4, 42; doi:10.3390/computation4040042

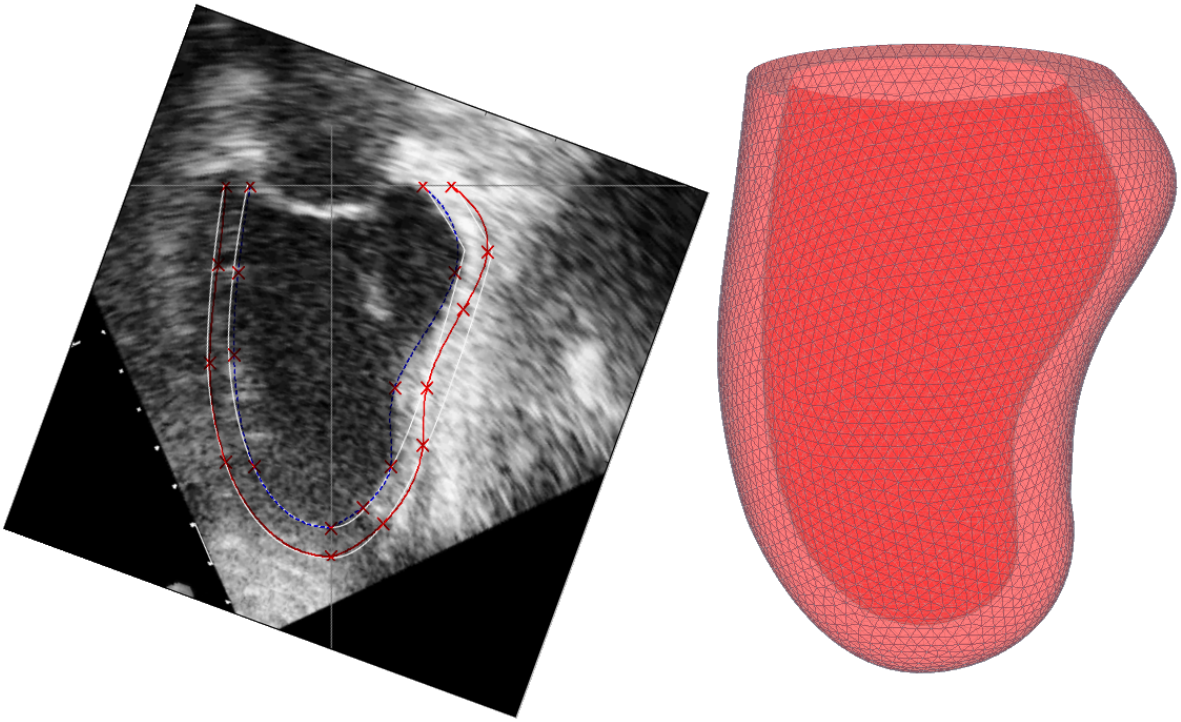

Figure 14. Ultrasound imaging as a base for model construction. *On the left*: a sonographical two-chamber view of a patient's heart and two measurements: the first for the power-function-based model (white lines) and the second for the spline-based model (blue lines show the endocardium; red lines show the epicardium). The patient suffered from an old myocardial infarction, and a scar is present. The marked points are shown as crosses. This view gives data for two model meridians. The model axis and base are shown as grey lines. The image has been rotated so that the model axis Oz is vertical. *On the right*: a spline-based model of this patient's LV. The view is semitransparent to show both the epicardial and endocardial surfaces. The surface mesh was made using Ani3D-AFT software [56].

The method to rarefy the computation mesh

Let us consider a mesh node with indices i, j, k of special coordinates γ, ψ, ϕ. In the case of the symmetric LV model, we propose that its γ- and ψ-neighbours have indices $i \pm 1$, $j \pm 1$. Its ϕ-neighbours have indices $k \pm Q[j]$, where Q is an array of natural numbers, and the differences are found so that the Cartesian distances between nodes are within some given limits. In the case of the non-symmetric LV model, we have to introduce six arrays instead of one, Q^{dir}_{var}, where $var \in \{\gamma, \psi, \phi\}$, $dir \in \{+1, -1\}$. The meaning of Q^{dir}_{var} is that the index of γ-neighbour of the node in direction dir is $i + dir \cdot Q^{dir}_{\gamma}$. The index of ψ-neighbour in direction dir is $j + dir \cdot Q^{dir}_{\psi}$. The index of ϕ-neighbour in direction dir is $k + dir \cdot Q^{dir}_{\phi}$. The values of Q have to be found once, at the initialization stage. If for a node (i, j, k) at least one of $Q^{dir}_{var}[i][j][k]$ cannot be found, this node is marked 'out-of-mesh'. We compute the potential in this node not by a finite difference method but by interpolation, using the node's closest 'in-mesh' neighbours.

The flowchart in Fig. 15 depicts all the steps of construction and the use of the model in electrophysiological simulations.

7. An example of the spline-based model's practical usage in electrophysiological simulations

The model was used to study the dynamics of scroll waves of electrical excitation. Such waves are solutions of classical reaction-diffusion systems, and they correspond to dangerous arrhythmias,

Preprints (www.preprints.org) | NOT PEER-REVIEWED | Posted: 20 October 2016 doi:10.20944/preprints201608.0080.v2

Peer-reviewed version available at Computation 2016, 4, 42; doi:10.3390/computation4040042

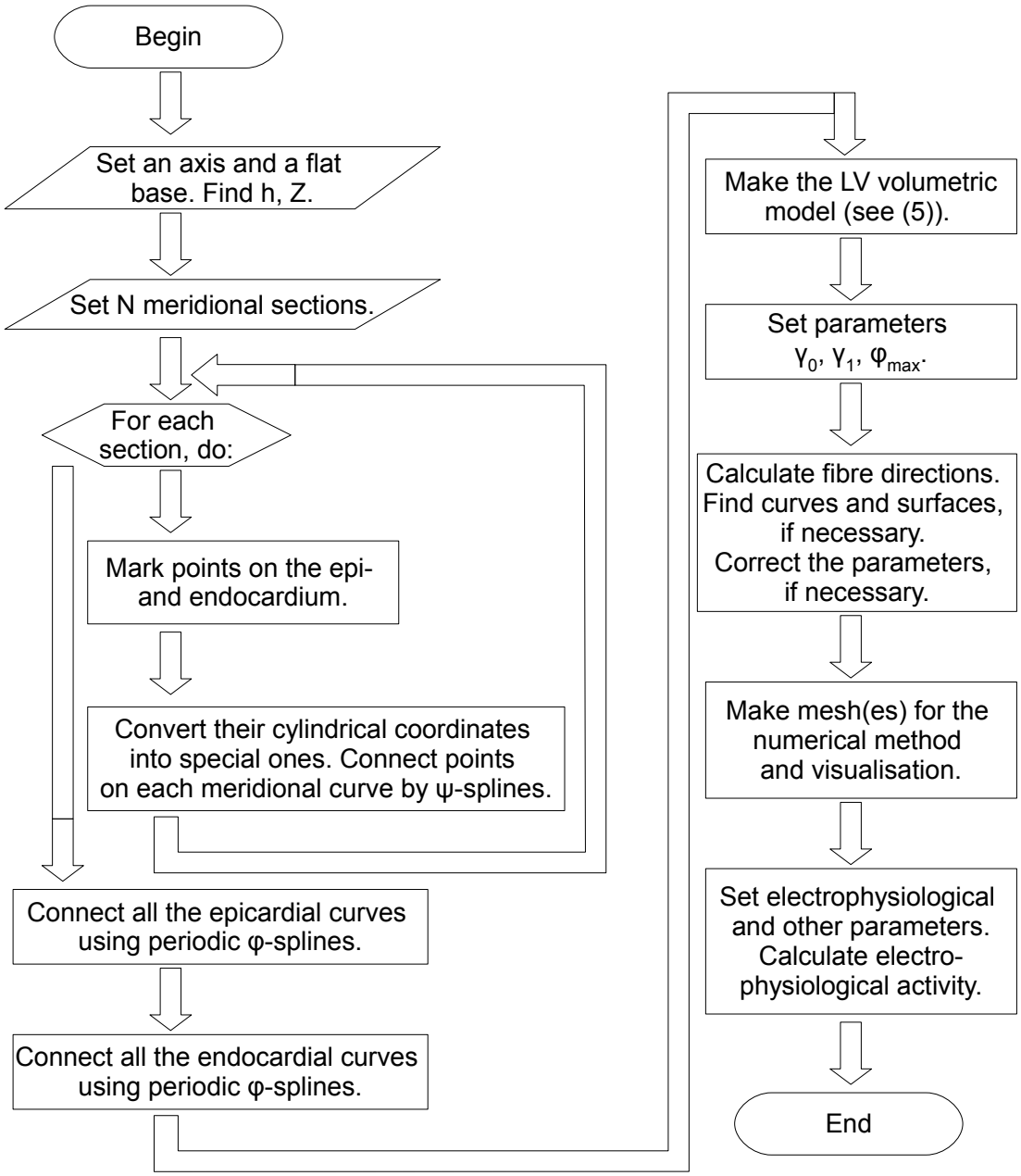

Figure 15. Flowchart displaying the steps for the construction and use of the spline-based LV model.

Preprints (www.preprints.org) | NOT PEER-REVIEWED | Posted: 20 October 2016 doi:10.20944/preprints201608.0080.v2

Peer-reviewed version available at Computation 2016, 4, 42; doi:10.3390/computation4040042

such as paroxysmal ventricular tachycardia and ventricular fibrillation. Our simulation was based on the Aliev–Panfilov model [60] of electrical excitation in the myocardium and the aforementioned human heart DT-MRI dataset and anatomical model (see Sections 2.4 and 4). The electrophysiological model is dimensionless and has the following form:

$$\begin{aligned} \frac{\partial u}{\partial t} &= \operatorname{div}(D \operatorname{grad} u) - ku(u-a)(u-1) - uv, \\ \frac{\partial v}{\partial t} &= \epsilon(u,v)(-v - ku(u-a-1)), \\ \epsilon(u,v) &= \epsilon_0 + \frac{\mu_1 v}{u+\mu_2}, \end{aligned} \tag{12}$$

where u is the transmembrane potential, v is the conductivity for the K current in the membrane, $D_{1,2}$ are diffusion coefficients along and across fibres, and k, a, ϵ_0, μ_1, μ_2 are cell model parameters. These parameters had the values $D_1 = 7.12$ mm^2/ms, $D_2 = D_1/9$, $k = 8$, $a = 0.1$, $\epsilon_0 = 0.01$, $\mu_1 = 0.12$, $\mu_2 = 0.3$. A boundary condition provided zero flux through the LV boundary. Initial conditions were $u = 1$, $v = 0$ (initial stimulation) at $\psi \le 0.4 \cdot \pi/2$, $0 \le \phi \le 2\pi/12$; $u = 0$, $v = k$ (initial temporary block of propagation) at $\psi \le 0.4 \cdot \pi/2$, $2\pi/12 \le \phi \le 2\pi/6$; and $u = 0$, $v = 0$ (resting state) elsewhere.

We used the spatial mesh size $dr = 0.5$ mm; the time step $dt = 0.01$ ms; and the dimension coefficients 5.4 ms, as the model time unit, and 6.2 mm, as the model length unit, based on the period and wavelength of a spiral wave simulated on a flat isotropic surface. The duration of the simulation was 10 sec.

The results we obtained are shown in Fig. 16, 17. From these results, we can see that the solitary filament drifted towards the base ($\psi = 0$), and then several filaments appeared. The number of filaments slowly increased from 1 to 9 and then decreased to 5-6. This observation means that a tachycardia paroxysm transformed into a fibrillation.

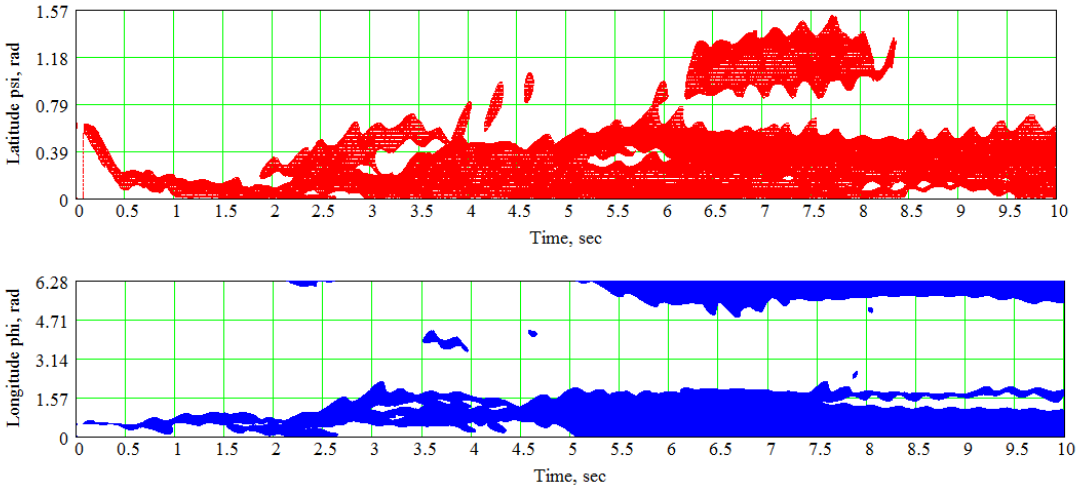

Figure 16. The special coordinates ψ and ϕ of the scroll wave filaments.

8. Discussion

This section analyses the algorithm, compares it with other models and techniques, examines its methods of verification, and concerns the usage and further development of the constructed model.

8.1. Advantages and disadvantages of the proposed model

The model adequately reproduces the fibre angles in the LV free wall and in the middle zone of the IVS of the human heart. Nevertheless, the data agreement in the apical zone of the IVS is only

Preprints (www.preprints.org) | NOT PEER-REVIEWED | Posted: 20 October 2016 doi:10.20944/preprints201608.0080.v2

Peer-reviewed version available at Computation 2016, 4, 42; doi:10.3390/computation4040042

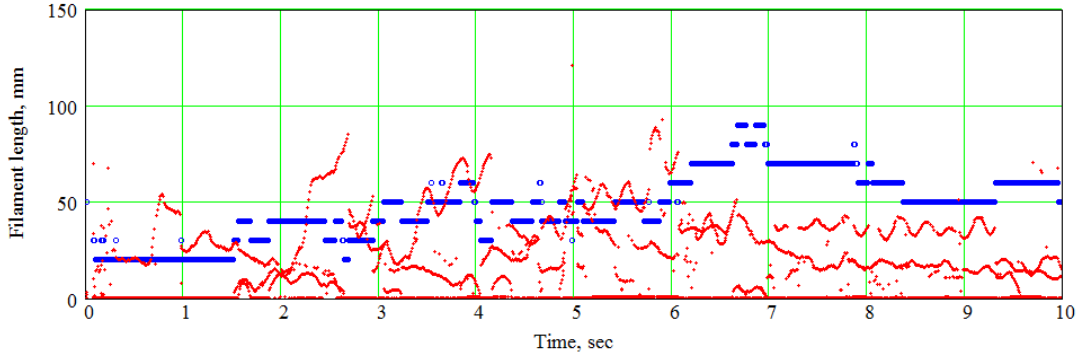

Figure 17. The number of filaments ($\times 10$; blue circles) and their lengths (red dots).

qualitative; in the IVS upper part of the human heart, the model yields results that differ from the experimental data.

Our model has the following merits:

- It has relatively few parameters for shape, fibres and sheets.
- The LV apex is smooth thanks to the special choice of function z. This is a useful feature for integration methods sensitive to the smoothness of the boundary.
- It uses only simple 1-variable splines, and no 2- or 3-parametric splines are required.
- The fitting of shape and fibre directions are independent tasks in this model.
- It is flexible enough to fit not only normal but pathological LVs.
- It yields not only fibres but also sheets.

Limitations of the model include the following:

- Similar to our previous models, its base is flat, which is not the case in real mammal anatomy.
- The fibres are not geodesic lines in the model sheets. It is difficult to determine if this is a disadvantage of the fibres, the sheets or both.
- Model fibres end at the base. However, this demerit can be amended by combining this model with the toroids-based one described in [61].
- It is unclear whether the model is generalisable for both ventricles.

8.2. The present model compared with other qualitative models

The ventrucilar myocardium's structure and its qualitative description have been explored for several centuries. Reviews of experimental findings and theoretical conceptions can be found, for example, in [23,62] and other reviews in the Supplementary Volume [63]. The present model is conceptually close to Krehl's nested toroids to the extent that the LV myocardium, except the papillary muscles, is filled by nonoverlapping surfaces, and each surface is filled by nonoverlapping curves. The distinctive feature of the proposed model is the spiral shape of the surfaces. Whether the SSs are close enough to real heart sheets is a topic for future research.

In [20], Streeter proposed the geodesic principle of winding fibres on the sheets. This principle holds in the toroidal model but not in the present one. However, if we keep the fibres only, the surfaces may be adjusted to them. This interesting problem remains for future research: How should we draw a set of nonoverlapping surfaces on the given set of curves so that the curves are geodesic on the surfaces?

Some qualitative models of the myocardium describe its structure on the levels of cells, myofibres and myolaminae (see, for example, [22,29,64]); such models examine interconnetions and arrangement of cardiomyocytes and other types of cardiac cells. However, the main task of our model is to yield fibre and sheet normal directions in all points of the LV myocardium but not to represent

the amazingly complex micro- and macrostructure of the cardiac muscle. A union of our model with a structural tissue-level model which includes Y-junctions of the cells, capillaries, fibrous tissue and other elements would be of great practical value.

A key feature of the proposed model is its numerical, quantitative nature, so it should be compared with other quantitative models and data.

8.3. Comparison with experimental data and quantitative models

Some experimental techniques that can be used to verify our model have been mentioned in our previous work [54]. These techniques include DT-MRI (already used here) as well as micro-CT [65], histological investigation [66] and quantitative polarised light microscopy [30]. These methods provide fibre orientation data that may be used for the construction of anatomical computational models in different ways.

- Finite-element models can utilise the data as a discrete dataset [13,67,68].
- Rule-based models, i.e. the models formed on the basis of some constitutive rule [44–47], can be compared against the data, which allows them to be verified.

A comparison with a recent rule-based method, the Laplace–Dirichlet algorithm [46], and with a wrapping-based myocardium model [69] was done in our previous paper [54]. The idea of using splines to fit cardiac imaging data is not new. An example of such LV shape model, constructed with B-splines, together with a review of spline-based models can be found in [70]. A common weak point of many such models, however, is a lack of computing fibre direction field.

A quantitative comparison with a model from [46] can be made by measuring the mean difference angle between the experimental and model data. Bayer et al. in [46] report that their result is $23^\circ \pm 20^\circ$. Our result on the human heart dataset is $21^\circ \pm 18^\circ$ and on the canine dataset it is $19.5^\circ \pm 14.1^\circ$, which is comparable with their achievement.

Our model fits the shape of the LV and has only three parameters (γ_0, γ_1, $\phi_{\max}$) to adapt fibre directions. Fibre directions can also be fitted through widely used fitting functions with many more parameters as it was done in [71]. In that work, fibre direction field in mice was approximated in spheroidal coordinates by a product of two algebraic and one trigonometric polynomials. A certain advantage of that approach is its flexibility. The reported root-mean-square error was about 2.3–10°. Yet, that method usually requires about 10 parameters for each algebraic and 10–40 for trigonometric polynomials, whereas our technique uses only 3 parameters. Also, the parameters in [71] have unclear geometrical or physical meaning, unlike ours. Moreover, the numbers of those parameters for different hearts vary, so the coefficients cannot be averaged to obtain *recommended* species-level parameter sets. We hope that our parameters can be averaged or fitted on the species level or at least for the norm and pathologies of particular species. This will allow researchers to construct fibre direction fields based on the shape of patients' hearts without DT-MRI data.

Let us discuss the level of model error in the fibre directions. How can local and global cardiac characteristics be affected if the fibre angles change?

In an article by Campbell et al. [72], electromechanics of dogs' hearts was modelled using different cell- and tussie-level parameter values. One of the authors' simulations included three models with different values of the total transmural fibre angle α_1, i.e. 112°, 145° and 170°, while all other parameters were the same. The mean transmural difference of the helix angle between the middle model and the extreme models was about 12°. The authors discovered that such fibre angle distribution affects the range of fibre strains and weakly changes haemodynamics and transmural delay in activation.

In a conference work by Wong et al. [73], the sensitivity of the average displacement of some points of the heart to epi- and endocardial fibre angles was studied. The angles were changed at increments of 20° from 20° to 80°. The analysis showed that a minimal change of the angle (though 20° is an essential angle) leads to a significant variation in displacement of the points. Our model has

Peer-reviewed version available at Computation 2016, 4, 42; doi:10.3390/computation4040042

special parameters for fitting the epi- and endocardial fibre angles, so such a significant average error in these angles is unlikely to appear.

In Sánchez's PhD thesis [74], linear and cubic laws of the helix fibre angle dependence on wall position were used in electromechanical simulations. The maximal difference between the angles was 23°, and it led to significant changes in maximal contraction time and total activation time.

Baron et al.'s conference paper [75] is focussed on the effect of fibre orientation on LV stroke volume. A change of 10° in epi- and endocardial helix angles leads to the following effects: an 18% difference in the atrioventricular plane displacement, quite a small difference ($\approx$ 2 mm Hg) in blood pressure in the LV, a 5% difference in the minimal LV-cavity volume, a 3.5% difference in the ejection fraction and a 2% difference in pressure-volume work.

Summarising all the aforementioned works, we conclude that fibre (helix) angle differences or errors on the order of 10° can sufficiently change the local parameters of cardiac activity but affect its global characteristics lightly.

The goal of our model is to predict the average field of fibre directions for a given species. Therefore, the model error has to lie in the intraspecies limits. For example, the limits reported in [72] for dog (12°) are close to the error achieved by our model (10.9°, see Table 1), which justifies the relevance of our technique.

8.4. Further development and usage of the model

The model does not include the uppermost part of the ventricular myocardium, the basal ring, where myofibres form torus-like shapes [28, Fig. 14]. Moreover, some of the data available on the apical region show that myofibres there make toroidal layers, similar to basal ones [28, Fig. 6].

This model has been constructed based on and verified against only two DT-MRI datasets, one canine and one human. Such validation is limited, so its development is an important topic of our future research.

The spline apparatus enables researchers to use this model in cases of complex wall geometry, such as in patients with old myocardial infarctions, and other situations where the wall has locuses of thickening and thinning.

The analytical description of cardiac geometry has been used in developing a new numerical method for the study of the electrophysiological activity of the LV. The model can also be utilised to generate different anisotropical properties of the heart, to alter the LV shape (by changing the model parameters) and to study their influence on cardiac electrical and mechanical functions.

Acknowledgments: The author is grateful to Tatyana V. Chumarnaya for providing the sonography image used in this work; to Anton A. Koshelev for his help with DT-MRI data scaling. This work is supported by The Russian Science Foundation (Project 14-35-00005).

Conflicts of Interest: The authors declare no conflict of interest. The founding sponsors had no role in the design of the study; in the collection, analyses, or interpretation of data; in the writing of the manuscript, and in the decision to publish the results.

Abbreviations

The following abbreviations are used in this manuscript:

CT: computed tomography
DT-MRI: diffusion tensor magnetic resonance imaging
DTI: diffuse tensor imaging
IVS: interventricular septum
LV: left ventricle
RV: right ventricle
SS: spiral surface

Bibliography

1. Trayanova, N.; Constantino, J.; Gurev, V. Electromechanical models of the ventricles. *Am J Physiol Heart Circ Physiol* **2011**, *301*, H279–H286.
2. Beyar, R.; Sideman, S. A computer study of the left ventricular performance based on fiber structure, sarcomere dynamics, and transmural electrical propagation velocity. *Circ Res* **1984**, *55*, 358–375.
3. Greenstein, J.; Winslow, R. Integrative systems models of cardiac excitation-contraction coupling. *Circ Res* **2011**, *108*, 70–84.
4. Hunter, P.; McCulloch, A.; Keurs, H.T. Modelling the mechanical properties of cardiac muscle. *Prog Biophys Mol Biol* **1998**, *69*, 289–331.
5. Tusscher, K.T.; Noble, D.; Noble, P.; Panfilov, A. A model for human ventricular tissue. *Am. J. Physiol. Heart Circ. Physiol.* **2004**, *286*, H1573–H1589.
6. Tusscher, K.T.; Panfilov, A. Alternans and spiral breakup in a human ventricular tissue model. *Am. J. Physiol. Heart Circ. Physiol.* **2006**, *291*, H1088–1100.
7. Grandi, E.; Pasqualini, F.; Bers, D. A novel computational model of the human ventricular action potential and Ca transient. *Journal of Molecular and Cellular Cardiology* **2010**, *48*, 112–121. Special Issue: Ion Channels.
8. O'Hara, T.; Virag, L.; Varro, A.; Rudy, Y. Simulation of the Undiseased Human Cardiac Ventricular Action Potential: Model Formulation and Experimental Validation. *PLoS Comput Biol* **2011**, *7*, e1002061.
9. Sulman, T.; Katsnelson, L.; Solovyova, O.; Markhasin, V. Mathematical modeling of mechanically modulated rhythm disturbances in homogeneous and heterogeneous myocardium with attenuated activity of $Na^+ - K^+$ pump. *Bull Math Biol.* **2008**, *70*, 910–949.
10. Niederer, S.; Hunter, P.; Smith, N. A quantitative analysis of cardiac myocyte relaxation: a simulation study. *Biophys J.* **2006**, *90*, 1697–1722.
11. Ter Keurs, H.; Shinozaki, T.; Zhang, Y.; Zhang, M.; Wakayama, Y.; Sugai, Y.; Kagaya, Y.; Miura, M.; Boyden, P.; Stuyvers, B.; Landesberg, A. Sarcomere mechanics in uniform and non-uniform cardiac muscle: a link between pump function and arrhythmias. *Prog Biophys Mol Biol.* **2008**, *97*, 312–331.
12. Rice, J.; de Tombe, P. Approaches to modeling crossbridges and calcium-dependent activation in cardiac muscle. *Prog Biophys Mol Biol.* **2004**, *85*, 179–195.
13. Gurev, V.; Lee, T.; Constantino, J.; Arevalo, H.; Trayanova, N. Models of cardiac electromechanics based on individual hearts imaging data: Image-based electromechanical models of the heart. *Biomech Model Mechanobiol* **2011**, *10*, 295–306.
14. Vetter, F.; McCulloch, A. Three-dimensional analysis of regional cardiac function: a model of rabbit ventricular anatomy. *Prog Biophys Mol Biol* **1998**, *69*, 157–183.
15. Nickerson, D.; Smith, N.; Hunter, P. New developments in a strongly coupled cardiac electromechanical model. *Europace* **2005**, *7*, 118–127.
16. Helm, P.; Tseng, H.; Younes, L.; McVeigh, E.; Winslow, R. Ex Vivo 3D Diffusion Tensor Imaging and Quantification of Cardiac Laminar Structure. *Magnetic Resonance in Medicine* **2005**, *54*, 850–859.
17. Lunkenheimer, P.; Redmann, K.; et al.. Three-Dimensional Architecture of the Left Ventricular Myocardium. *The Anatomical Record Part A* **2006**, *288*, 565–578.
18. Helm, P.; Beg, M.; Miller, M.; Winslow, R. Measuring and mapping cardiac fiber and laminar architecture using diffusion tensor MR imaging. *Ann N Y Acad Sci.* **2005**, *1047*, 296–307.
19. Vadakkumpadan, F.; Arevalo, H.; Prassl, A.; et al. Image-based models of cardiac structure in health and disease. *Wiley Interdiscip. Rev. Syst. Biol. Med.* **2010**, *2*, 489–506.
20. Streeter, D., Handbook of physiology. Sec. 2. Vol. I. The Heart; Bethesda, Maryland: Am. Physiol. Soc, 1979; chapter Gross morphology and fiber geometry of the heart, pp. 61–112.
21. Nielsen, P.; LeGrice, I.; Smaill, B.; Hunter, P. Mathematical model of the geometry and fibrous structure of the heart. *Am. J. Physiol.* **1991**, *260*, H1365–H1378.
22. LeGrice, I.; Smaill, B.; Chai, L.; Edgar, S.; Gavin, J.; Hunter, P. Laminar structure of the heart: ventricular myocyte arrangement and connective tissue architecture in the dog. *Am J Physiol* **1995**, *269*, H571–582.
23. Gilbert, S.H.; Benson, A.P.; Li, P.; Holden, A.V. Regional localisation of left ventricular sheet structure: integration with current models of cardiac fibre, sheet and band structure. *European Journal of Cardio-Thoracic Surgery* **2007**, *32*, 231–249.
24. Frangi, A.; Rueckert, D.; Schnabel, J.; Niessen, W. Automatic construction of multiple-object three-dimensional statistical shape models: application to cardiac modeling. *IEEE Transact on Med Imag* **2002**, *21*, 1151–1166.

25. Young, A.; Frangi, A. Computational cardiac atlases: from patient to population and back. *Exp Physiol* **2009**, *94*, 578–596.
26. Peyrat, J.; Sermesant, M.; Pennec, X.; Delingette, H.; Xu, C.; McVeigh, E.; Ayac, N. Towards a Statistical Atlas of Cardiac Fiber Structure. *LNCS* **2006**, *4190*, 297–304.
27. Peyrat, J.; Sermesant, M.; Pennec, X.; Delingette, H.; Xu, C.; McVeigh, E.; Ayache, N. A computational framework for the statistical analysis of cardiac diffusion tensors: application to a small database of canine hearts. *IEEE Transact on Med Imag* **2007**, *26*, 1500–1514.
28. Torrent-Guasp, F. *The Cardiac Muscle*; Madrid: Fundacion Juan March, 1973.
29. Rushmer, R.; Crystal, D.; Wagner, C. The functional anatomy of ventricular contraction. *Circ Res* **1953**, *1*, 162–170.
30. Jouk, P.; Usson, Y.; Michalowicz, G.; Grossi, L. Three-dimensional cartography of the pattern of the myofibres in the second trimester fetal human heart. *Anat Embryol (Berl).* **2000**, *202*, 103–118.
31. Mall, F. On the muscular architecture of the ventricles of the human heart. *Am J Anat.* **1911**, *11*, 211–266.
32. Benninghoff, A. Die Architektur des Herzmuskels. Eine vergleichend anatomische und vergleichend funktionelle Betrachtung. *Morph Jahrb.* **1931**, *67*, 262–317.
33. Robb, J.; Robb, R. The normal heart. Anatomy and physiology of the structural units. *Am Heart J.* **1942**, *23*, 455–467.
34. Lev, M.; Simkins, C. Architecture of the human ventricular myocardium. Technique for study using a modification of the Mall–MacCallum method. *Lab Invest.* **1956**, *5*, 396–409.
35. Torrent-Guasp, F., El Fallo Mecanico del Corazon; Ediciones Toray, Barcelona, 1975; chapter Organizacion de la musculatura cardiaca ventricular, pp. 3–36.
36. Lunkenheimer, P.; Redmann, K.; Scheld, H.; Dietl, K.H.; Cryer, C.; Richter, K.D.; Merker, J.; Whimster, W. The heart muscle's putative "secondary structure". Functional implications of a band-like anisotropy. *Technol Health Care* **1997**, *5*, 53–64.
37. Schmid, P.; Niedered, P.; Lunkenheimer, P.; Torrent-Guasp, F. The anisotropic structure of the human left and right ventricles. *Technol Health Care* **1997**, *5*, 29–44.
38. Torrent-Guasp, F.; Whimster, W.; Redman, K. A silicone rubber mould of the heart. *Technol Health Care* **1997**, *5*, 13–20.
39. Hort, W. Makroskopische und mikrometrische Untersuchungen am Myokard verschieden stark gefüllter linker Kammern. *Virchows Arch Pathol Anat* **1960**, *333*, 523–564.
40. Hort, W. Quantitative morphology and structural dynamics of the myocardium. *Methods Achiev Exp Pathol* **1971**, *5*, 3–21.
41. Fox, C.; Hutchins, G. The architecture of the human ventricular myocardium. *Hopkins Med J* **1972**, *130*, 289–299.
42. Krehl, L. Beiträge zur Kenntnis der Füllung und Entleerung des Herzens. *Abh Math-Phys Kl Saechs Akad Wiss* **1891**, *17*, 341–362.
43. Grant, R. Notes on the muscular architecture of the left ventricle. *Circulation* **1965**, *32*, 301–308.
44. Seemann, G. Modeling of Electrophysiology and Tension Development in the Human Heart. PhD thesis, Universitat Karlsruhe, 2005.
45. Bishop, M.J.; Plank, G.; Burton, R.A.B.; Schneider, J.E.; Gavaghan, D.J.; Grau, V.; Kohl, P. Development of an anatomically detailed MRI-derived rabbit ventricular model and assessment of its impact on simulations of electrophysiological function. *Am J Physiol Heart Circ Physiol.* **2010**, *298*, H699–H718.
46. Bayer, J.; Blake, R.; Plank, G.; Trayanova, N. A Novel Rule-Based Algorithm for Assigning Myocardial Fiber Orientation to Computational Heart Models. *Ann Biomed Eng.* **2012**.
47. Hren, R. A Realistic Model of the Human Ventricular Myocardium: Application to the Study of Ectopic Activation. PhD thesis, Halifax, Nova Scotia, Canada: Dalhousie University, 1996.
48. Peskin, C. Fiber architecture of the left ventricular wall: An asymptotic analysis. *Communications on Pure and Applied Mathematics* **1989**, *42*, 79–113.
49. Chadwick, R. Mechanics of the left ventricle. *Biophysical Journal* **1982**, *39*, 279–288.
50. Bovendeerd, P.; Arts, T.; Huyghe, J.; Campen, D.V.; Reneman, R. Dependence of local left ventricular wall mechanics on myocardial fiber orientation: a model study. *J Biomechanics* **1992**, *25*, 1129–1140.
51. Arts, T.; Veenstra, P.; Reneman, R. Epicardial deformation and left ventricular wall mechanics during ejection in the dog. *Am J Physiol* **1982**, *243*, H379–H390.

52. Pettigrew, J. On the arrangement of the muscular fibers of the ventricular portion of the heart of the mammal. *Proc. Roy. Soc., London* **1860**, *10*, 433–440.
53. Pravdin, S.; Berdyshev, V.; Panfilov, A.; Katsnelson, L.; Solovyova, O.; Markhasin, V. Mathematical Model of the Anatomy and Fibre Orientation Field of the Left Ventricle of the Heart. *Biomedical Engineering Online* **2013**, *54*, 1–21.
54. Pravdin, S. Non-axisymmetric mathematical model of the cardiac left ventricle anatomy. *Russian Journal of Biomechanics* **2013**, *17*, 75–94.
55. http://www.biomecardio.com/matlab/smoothn.html.
56. Advanced Numerical Instruments 3D - Ani3D. https://sourceforge.net/projects/ani3d/.
57. Pravdin, S.; Dierckx, H.; Katsnelson, L.; Solovyova, O.; Markhasin, V.; Panfilov, A. Electrical Wave Propagation in an Anisotropic Model of the Left Ventricle Based on Analytical Description of Cardiac Architecture. *PLOS One* **2014**, *9*, e93617. doi:10.1371/journal.pone.0093617.
58. Pravdin, S.; Dierckx, H.; Markhasin, V.; Panfilov, A. Drift of scroll wave filaments in an anisotropic model of the left ventricle of the human heart. *Biomed Research International Journal* **2015**, *2015*, 1–13.
59. Pravdin, S. A method of solving reaction-diffusion problem on a non-symmetrical model of the cardiac left ventricle. Proceedings of the 47th International Youth School-conference «Modern Problems in Mathematics and its Applications», Yekaterinburg, Russia. IMM Urb RAS, Yekaterinburg, 2016, pp. 284–296.
60. Aliev, R.; Panfilov, A. A simple two-variable model of cardiac excitation. *Chaos, Solitons and Fractals* **1996**, *7*, 293–301.
61. Koshelev, A.; Pravdin, S.; Ushenin, K.; Bazhutina, A.; Katsnelson, L.; Solovyova, O. A modified mathematical model of the anatomy of the cardiac left ventricle. *Biofizika* **2016**, *61*. accepted; in Russian.
62. Kocica, M.J.; Corno, A.F.; Carreras-Costa, F.; Ballester-Rodes, M.; Moghbel, M.C.; Cueva, C.N.; Lackovic, V.; Kanjuh, V.I.; Torrent-Guasp, F. The helical ventricular myocardial band: global, three-dimensional, functional architecture of the ventricular myocardium. *European Journal of Cardio-Thoracic Surgery* **2006**, *29*, S21–S40.
63. Rethinking the Cardiac Helix: A Structure/Function Journey, 2006. European Journal of Cardio-Thoracic Surgery, Vol. 29, S1.
64. Anderson, R.H.; Ho, S.Y.; Redmann, K.; Sanchez-Quintana, D.; Lunkenheimer, P.P. The anatomical arrangement of the myocardial cells making up the ventricular mass. *European Journal of Cardio-Thoracic Surgery* **2005**, *28*, 517–525, [http://ejcts.oxfordjournals.org/content/28/4/517.full.pdf+html].
65. Aslanidi, O.; Nikolaidou, T.; Zhao, J.; Smaill, B.; Gilbert, S.; Holden, A.; Lowe, T.; Withers, P.; Stephenson, R.; Jarvis, J.; Hancox, J.; Boyett, M.; Zhang, H. Application of Micro-Computed Tomography With Iodine Staining to Cardiac Imaging, Segmentation, and Computational Model Development. *Medical Imaging, IEEE Transactions on* **2013**, *32*, 8–17.
66. Trew, M.; Caldwell, B.; Sands, G.; LeGrice, I.; Smaill, B. Three-dimensional cardiac tissue image registration for analysis of in vivo electrical mapping. *Ann Biomed Eng* **2011**, *39*, 235–248.
67. Vicky, Y.W. Modelling In Vivo Cardiac Mechanics using MRI and FEM. PhD thesis, Auckland Bioengineering Institute, The University of Auckland, New Zealand, 2012.
68. Zhang, Y.; Liang, X.; Ma, J.; Jing, Y.; Gonzales, M.J.; Villongco, C.; Krishnamurthy, A.; Frank, L.R.; Nigam, V.; Stark, P.; Narayan, S.M.; McCulloch, A.D. An atlas-based geometry pipeline for cardiac Hermite model construction and diffusion tensor reorientation. *Medical Image Analysis* **2012**, *16*, 1130–1141.
69. Sinha, S.; Stein, K.M.; Christini, D.J. Critical role of inhomogeneities in pacing termination of cardiac reentry. *Chaos: An Interdisciplinary Journal of Nonlinear Science* **2002**, *12*, 893–902.
70. Li, J.; Denney, T.S.J. Left ventricular motion reconstruction with a prolate spheroidal B-spline model. *Physics in Medicine and Biology* **2006**, *51*, 517–537.
71. Merchant, S.S.; Gomez, A.D.; Morgan, J.L.; Hsu, E.W. Parametric modeling of the mouse left ventricular myocardial fiber structure. *Annals of Biomedical Engineering* **2016**.
72. Campbell, S.G.; Howard, E.; Aguado-Sierra, J.; Coppola, B.A.; Omens, J.H.; Mulligan, L.J.; McCulloch, A.D.; Kerckhoffs, R.C.P. Effect of transmurally heterogeneous myocyte excitation-contraction coupling on canine left ventricular electromechanics. *Experimental Physiology* **2009**, *94*, 541–552.
73. Wong, K.C.L.; Billet, F.; Mansi, T.; Chabiniok, R.; Sermesant, M.; Delingette, H.; Ayache, N., Cardiac Motion Estimation Using a ProActive Deformable Model: Evaluation and Sensitivity Analysis. In

Statistical Atlases and Computational Models of the Heart: First International Workshop, STACOM 2010, and Cardiac Electrophysiological Simulation Challenge, CESC 2010, Held in Conjunction with MICCAI 2010, Beijing, China, September 20, 2010. Proceedings; Springer Berlin Heidelberg: Berlin, Heidelberg, 2010; pp. 154–163.

74. Sánchez, R.A. Electromechanical Large Scale Computational Models of the Ventricular Myocardium. PhD thesis, Universitat Politecnica de Catalunya, 2014.
75. Baron, L.; Fritz, T.; Seemann, G.; Dössel, O. Sensitivity study of fiber orientation on stroke volume in the human left ventricle. Computing in Cardiology 2014, 2014, pp. 681–684.

Appendix Calculation of the fibre direction in points of the LV model

In practical applications of cardiac anatomical models, it is necessary to compute a vector of fibre direction in a point whose position is given in a Cartesian coordinate system. Let the point coordinates be (x, y, z). One can easily convert them into cylindrical coordinates (ρ, ϕ, z). The vector of fibre direction can be found using the following algorithm:

1. Use formula (5) to find the special coordinates γ and ψ of the point numerically. This problem can be reduced to solving one algebraic equation with one unknown quantity γ on the segment $[0, 1]$. We utilise the expression for $\psi(\gamma, z)$ from formula (1) and substitute it into (5):

$$\rho = \rho^{epi}(\psi(\gamma, z), \phi)(1 - \gamma) + \rho^{endo}(\psi(\gamma, z), \phi)\gamma.$$

   We solve this equation with respect to γ. Let the root be γ. Hence, the point's special coordinate $\psi = \arcsin\left(\frac{Z-z}{Z-h\gamma}\right)$.
2. Differentiate (numerically or analytically) the function $\rho(\gamma, \psi, \phi)$ with respect to all arguments and obtain three partial derivatives ρ_γ, ρ_ψ, and ρ_ϕ. We can find one derivative analytically:

$$\rho_\gamma = \rho^{endo}(\psi, \phi) - \rho^{epi}(\psi, \phi).$$

3. The LV model point is an image of a point on the sector $\mathrm{P} \le 1$, $\Phi \in [\pi\gamma_0, \pi\gamma_1]$. This point, the preimage, has polar coordinates $\mathrm{P} = 1 - \frac{2\psi}{\pi}$, $\Phi = \pi\gamma(\gamma_1 - \gamma_0) + \pi\gamma_0$ and Cartesian coordinates $X = \mathrm{P}\cos\Phi$, $Y = \mathrm{P}\sin\Phi$.
4. The LV point $\vec{r}$, parameterised by Φ, has Cartesian coordinates

$$x(\Phi) = \rho(\gamma(\Phi), \psi(\mathrm{P}(\Phi)), \phi(\gamma(\Phi), \phi_{\min}, \phi_{\max}))\cos\phi(\gamma(\Phi), \phi_{\min}, \phi_{\max}),$$

$$y(\Phi) = \rho(\gamma(\Phi), \psi(\mathrm{P}(\Phi)), \phi(\gamma(\Phi), \phi_{\min}, \phi_{\max}))\sin\phi(\gamma(\Phi), \phi_{\min}, \phi_{\max}),$$

$$z(\Phi) = \rho(\gamma(\Phi), \psi(\mathrm{P}(\Phi))),$$

   where $\phi_{\min} = \phi - \gamma\phi_{\max}$, $\mathrm{P}(\Phi) = Y / \sin\Phi$.
5. The non-normalized vector $\vec{w} = (wx, wy, wz) = \frac{d\vec{r}}{d\Phi}$ of the fibre direction has components

$$wx = \frac{\sin\Phi}{(\pi - 2\psi)(\gamma_1 - \gamma_0)} \cdot \left(y\phi_{\max} - (\rho_\gamma + \rho_\phi\phi_{\max}) \cdot \cos\phi\right) - \cos\phi \cdot \rho_\psi \cdot \frac{\pi}{2} \cdot \cos\Phi,$$

$$wy = \frac{\sin\Phi}{(2\psi - \pi)(\gamma_1 - \gamma_0)} \cdot \left(x\phi_{\max} + (\rho_\gamma + \rho_\phi\phi_{\max}) \cdot \sin\phi\right) - \sin\phi \cdot \rho_\psi \cdot \frac{\pi}{2} \cdot \cos\Phi,$$

$$wz = \frac{h\sin\Phi\sin\psi}{(2\psi - \pi)(\gamma_1 - \gamma_0)} + (Z - h\gamma)\cos\psi \cdot \frac{\pi}{2} \cdot \cos\Phi.$$

Preprints (www.preprints.org) | NOT PEER-REVIEWED | Posted: 20 October 2016 doi:10.20944/preprints201608.0080.v2

Peer-reviewed version available at Computation 2016, 4, 42; doi:10.3390/computation4040042

Appendix Formulae for the Laplacian in the special coordinates

Let us denote the special coordinates (γ, ψ, ϕ) uniformly as (ξ_0, ξ_1, ξ_2) and consider matrices

$$\mathbf{J} = (J_{ij}) = \left(\frac{\partial \xi_i}{\partial x_j}\right),$$
$$\mathbf{W} = (W_{ij}) = \left(\frac{\partial v_i}{\partial x_j}\right), \qquad \mathbf{S} = (S_{ij}) = \left(\frac{\partial v_i}{\partial \xi_j}\right),$$
$$\mathbf{T}^k = (T^k_{ij}) = \left(\frac{\partial^2 \xi_k}{\partial x_i \, \partial x_j}\right), \qquad \mathbf{H}^k = (H^k_{ij}) = \left(\frac{\partial^2 x_k}{\partial \xi_i \, \partial \xi_j}\right),$$

where $v = (v_0, v_1, v_2)$ is the unit fibre direction vector. These matrices are linked by the relations

$$\mathbf{W} = \mathbf{S}\mathbf{J},$$
$$T^k_{mp} = -\sum_l J_{kl} (\mathbf{J}^T \mathbf{H}^l \mathbf{J})_{mp}.$$

The Laplacian can be written as

$$\operatorname{div}(\mathbf{D} \operatorname{grad} u) = \sum_k p_k \cdot \frac{\partial u}{\partial \xi_k} + \sum_{k,l} q_{kl} \cdot \frac{\partial^2 u}{\partial \xi_k \, \partial \xi_l},$$

where

$$p_k = D_2 \operatorname{tr} \mathbf{T}^k + (D_1 - D_2) \cdot \Big((\mathbf{J}\mathbf{v})_k \cdot \operatorname{tr}(\mathbf{S}\mathbf{J}) + (\mathbf{J}\mathbf{S}\mathbf{J}\mathbf{v})_k + \mathbf{v}^{\mathrm{T}} \mathbf{T}^k \mathbf{v} \Big),$$

and q_{kl} are elements of matrix $\mathbf{Q}$:

$$\mathbf{Q} = \mathbf{J}\mathbf{D}\mathbf{J}^{\mathrm{T}}.$$

Appendix The no-flux boundary conditions in the special coordinates

The boundary condition

$$\mathbf{n}\mathbf{D} \operatorname{grad} u = 0, \tag{13}$$

where $\mathbf{n}$ is the normal vector to the LV surface, can be written in the form

$$\mathbf{n}^{\mathrm{T}} \mathbf{D} \mathbf{J}^{\gamma} \frac{\partial u}{\partial \gamma} + \mathbf{n}^{\mathrm{T}} \mathbf{D} \mathbf{J}^{\psi} \frac{\partial u}{\partial \psi} + \mathbf{n}^{\mathrm{T}} \mathbf{D} \mathbf{J}^{\varphi} \frac{\partial u}{\partial \varphi} = 0, \tag{14}$$

where $\mathbf{J}^{\gamma,\psi,\varphi}$ are the vector-columns of derivatives of the special coordinates with respect to Cartesian ones:

$$\mathbf{J}^{\gamma} = \begin{pmatrix} \gamma_x \\ \gamma_y \\ \gamma_z \end{pmatrix}$$

and so on. We use the method of fictitious nodes and make an additional layer of nodes outside the LV model. Values of the potential are found based on first-order derivatives with respect to the special coordinates. This method allows us to calculate the Laplacian in all non-fictitious nodes, be it points on the LV boundary or in its depth, on a consistent basis.

For the endo- and epicardium, equation (14) has to be solved for $\frac{\partial u}{\partial \gamma}$. Then, we find the potential at the fictitious node behind the endocardium (in the LV cavity) or the epicardium, respectively.

For the LV base, we transform equation (13) to form

$$\sum_k \left(\sum_j D^{2j} \frac{\partial \xi_k}{\partial x_j} \right) \frac{\partial u}{\partial \xi_k} = 0,$$

and express $\frac{\partial u}{\partial \psi}$:

$$\frac{\partial u}{\partial \psi} = -\frac{\left(D^{20}\gamma_x + D^{21}\gamma_y + D^{22}\gamma_z\right)\frac{\partial u}{\partial \gamma} + \left(D^{20}\varphi_x + D^{21}\varphi_y + D^{22}\varphi_z\right)\frac{\partial u}{\partial \varphi}}{D^{20}\psi_x + D^{21}\psi_y + D^{22}\psi_z}.$$

The required derivatives can be found numerically. The fictitious node is located above the LV base.